HEALTH AND MEDICINE

Engineered MgO nanoparticles for cartilage-bone synergistic therapy

Liming Zheng[1,2,3,4]†, Sheng Zhao[2]†, Yixuan Li[1]†, Jiankun Xu[5], Wenjin Yan[1], Baosheng Guo[1], Jianbin Xu[3], Lifeng Jiang[3], Yifeng Zhang[1,4]*, Hui Wei[2]*, Qing Jiang[1]*

The emerging therapeutic strategies for osteoarthritis (OA) are shifting toward comprehensive approaches that target periarticular tissues, involving both cartilage and subchondral bone. This shift drives the development of single-component therapeutics capable of acting on multiple tissues and cells. Magnesium, an element essential for maintaining skeletal health, shows promise in treating OA. However, the precise effects of magnesium on cartilage and subchondral bone are not yet clear. Here, we investigated the therapeutic effect of Mg^{2+} on OA, unveiling its protective effects on both cartilage and bone at the cellular and animal levels. The beneficial effect on the cartilage-bone interaction is primarily mediated by the PI3K/AKT pathway. In addition, we developed poly(lactic-*co*-glycolic acid) (PLGA) microspheres loaded with nano-magnesium oxide modified with stearic acid (SA), MgO&SA@PLGA, for intra-articular injection. These microspheres demonstrated remarkable efficacy in alleviating OA in rat models, highlighting their translational potential in clinical applications.

INTRODUCTION

Osteoarthritis (OA) is a prevalent joint disorder that affects over 250 million individuals worldwide (*1*, *2*). With the rapid increases in global aging, obesity, and knee trauma, further escalation of medical burden of OA is anticipated (*3*). Notably, the pathogenesis of OA is complex, primarily because it affects the periarticular tissues (*4*). With the advances in molecular classification, OA has been classified into cartilage degradation–driven, bone remodeling–driven, pain-driven, and inflammation-driven subtypes depending on the representative altered molecules. These subtypes are not necessarily mutually exclusive, and a combination of treatments targeting different mechanisms may therefore be effective (*5*). The combined use of various agents, such as diverse growth factors and small molecules, has the potential to target multiple tissues concurrently (*6*–*8*). These agents were applied in the treatment of OA via cartilage tissue engineering, such as through hydrogels (*9*, *10*). However, the industrial production and clinical application of these agents are limited by their complex manufacturing techniques, high cost, and side effects (*11*, *12*). Therefore, it is important to develop cost-effective, single-component therapeutics that can directly regulate multiple tissues.

Magnesium (Mg) is an element that is mainly stored in the skeletal system and plays a crucial role in maintaining bone and cartilage health (*13*–*16*). Previous studies have revealed the link between magnesium ion (Mg^{2+}) deficiency and the progression of OA (*17*, *18*). Notably, oral and intra-articular Mg^{2+} supplementation has shown beneficial effects in OA treatment (*19*–*21*). The intra-articular injection of $MgCl_2$ solution effectively protects cartilage from damage in OA rats. In the progression of OA, the balance between cartilage and bone formation and resorption is mainly influenced by three cell types, including bone marrow mesenchymal stem cells (BMSCs), chondrocytes, and osteoclasts (*22*). As a ubiquitous element found in almost all cell types, Mg^{2+} has been shown to effectively stabilize enzymes and nucleic acids, thereby exerting therapeutic effects on various cells in OA (*23*). Thus, Mg^{2+} may attenuate OA by acting on various cell types, but the precise therapeutic mechanism of Mg^{2+} remains obscure.

In this work, we proposed two hypothesis and verified them. One is that Mg^{2+} could synergically regulate subchondral bone and cartilage to treat OA. The other is that the regulation of different behaviors of BMSCs, chondrocytes, and monocytes could be related to the regulation of one key protein, AKT. The findings revealed that Mg^{2+} promoted chondrogenic differentiation and inhibited osteogenic differentiation of BMSCs. Furthermore, it inhibited cellular apoptosis in chondrocytes and the formation of osteoclasts through the AKT-related pathway. At the tissue level, Mg^{2+} exhibited protective effects on cartilage and subchondral bone. To effectively deliver an appropriate concentration of Mg^{2+} to the joint cavity in vivo, we used magnesium oxide (MgO) as a precursor for Mg^{2+} and poly(lactic-*co*-glycolic acid) (PLGA) as a carrier. The Mg^{2+}-containing delivery system showed stable release of Mg^{2+} in the joint cavity without altering the local acid-base environment. The administration of MgO nanoparticles loaded into PLGA microparticles (MPs) in the joint cavity effectively relieved the progression of OA, while the cartilage and subchondral bone were simultaneously affected (Fig. 1).

[1]Division of Sports Medicine and Adult Reconstructive Surgery, Department of Orthopedic Surgery, Nanjing Drum Tower Hospital, Affiliated Hospital of Medical School, Nanjing University, 321 Zhongshan Road; State Key Laboratory of Pharmaceutical Biotechnology, Nanjing University; Branch of National Clinical Research Center for Orthopedics, Sports Medicine and Rehabilitation; Institute of Medical 3D Printing, Nanjing University; Jiangsu Engineering Research Center for 3D Bioprinting, Nanjing 210008, Jiangsu, PR China. [2]Department of Biomedical Engineering, College of Engineering and Applied Sciences, Nanjing National Laboratory of Microstructures, Jiangsu Key Laboratory of Artificial Functional Materials, Nanjing University; State Key Laboratory of Analytical Chemistry for Life Science, School of Chemistry and Chemical Engineering, Chemistry and Biomedicine Innovation Center (ChemBIC), Nanjing University, Nanjing 210023, Jiangsu, PR China. [3]Department of Orthopedic Surgery, The Second Affiliated Hospital, Zhejiang University School of Medicine; Orthopedics Research Institute of Zhejiang University; Key Laboratory of Motor System Disease Research and Precision Therapy of Zhejiang Province; Clinical Research Center of Motor System Disease of Zhejiang Province, Hangzhou, Zhejiang, 310000, PR China. [4]School of Life Science and Technology, ShanghaiTech University, Shanghai, 201210, PR China. [5]Musculoskeletal Research Laboratory, Department of Orthopedics and Traumatology, The Chinese University of Hong Kong, Hong Kong 999077, PR China.
*Corresponding author. Email: zhangyf3@shanghaitech.edu.cn (Y.Z.); weihui@nju.edu.cn (H.W.); qingj@nju.edu.cn (Q.J.)
†These authors contributed equally to this work.

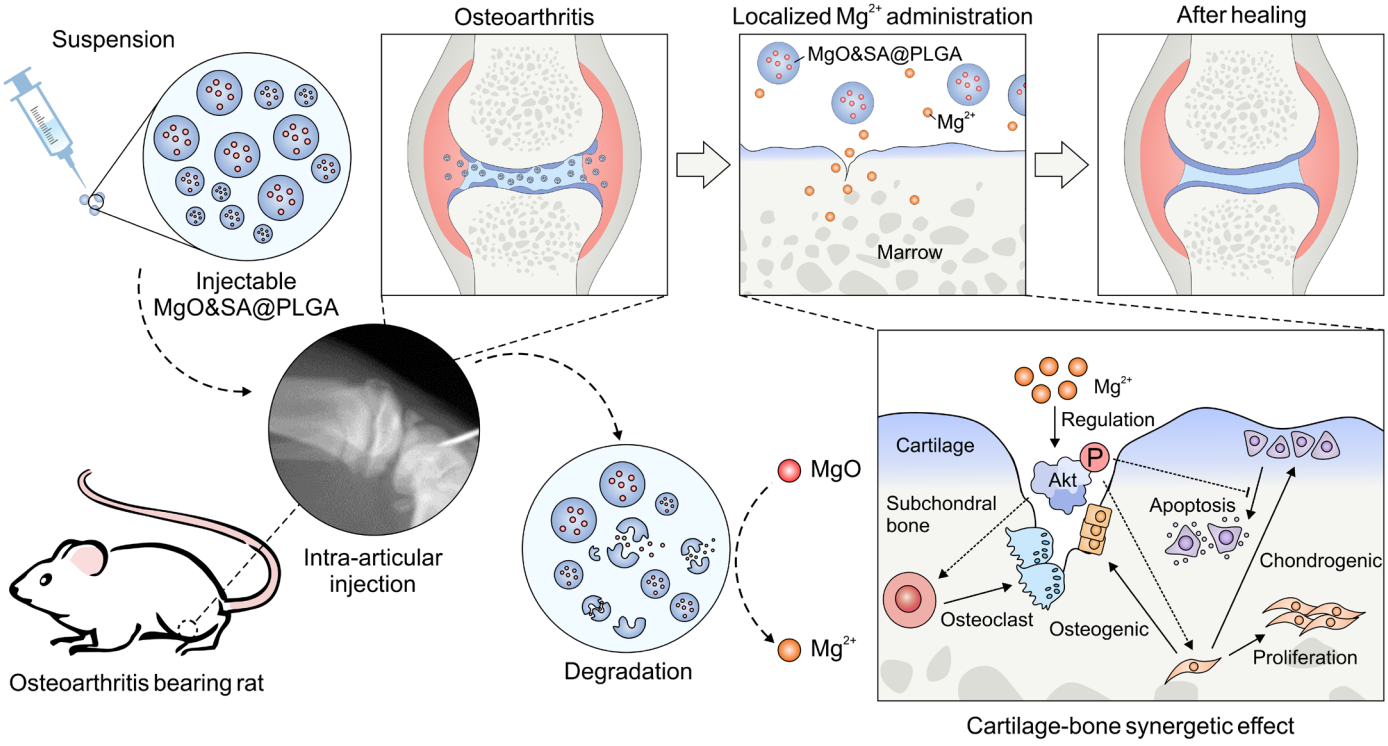

Fig. 1. Schematic illustration. We fabricated MgO&SA@PLGA and performed intra-articular injection of MgO&SA@PLGA in rats. The sustainably released Mg^{2+} promoted proliferation and chondrogenic differentiation of BMSCs, inhibited the formation of osteoblasts and osteoclasts via regulating the phosphorylation of AKT, and protected cartilage and subchondral bone from osteoarthritic damage in vivo.

RESULTS

Mg^{2+} reduces the degeneration of human tissues ex vivo

Before evaluating the therapeutic effect of Mg^{2+} in OA, we first conducted in vitro studies using ATDC5 and SW1353 cells to investigate the biocompatibility of Mg^{2+}. Through morphological observations and CCK-8 tests, we showed that Mg^{2+} was safe when its concentration did not exceed 20 mM in both inflammatory and noninflammatory environments (fig. S1, A to C). Therefore, for the subsequent experiments, concentrations lower than or equal to 20 mM were selected.

Cartilage tissues were obtained from 13 participants who met the inclusion and exclusion criteria (fig. S2). The detailed demographic information of the participants is summarized in table S1. As shown in Fig. 2A, the OA cartilage tissues were collected from the medial tibial plateau and subsequently cultured ex vivo. Both immunostaining and Western blot results revealed that the expression of COL2A1 and SOX9 increased after treated with 10 mM Mg^{2+}, while the expression of COL1A2 showed no significant differences, indicating no altered mineralization (Fig. 2, B to F). In addition, the expression of COL10A1 significantly decreased after treatment, indicating that hypertrophy was inhibited (Fig. 2, E and F). After treatment with 10 mM Mg^{2+} for 0, 4, 24, and 72 hours, Western blot results revealed that the expression of COL2A1 and SOX9 increased to different degrees. The expression of SOX9 increased rapidly between 0 and 4 hours, while the expression of COL2A1 gradually increased and reached a plateau at about 24 hours (Fig. 2, G and H). The expression of COL1A2 did not significantly change, while the expression of COL10A1 significantly decreased, which is according to the results in 24 hours. These findings demonstrate that 10 mM Mg^{2+} effectively rescues the OA damage of cartilage tissue ex vivo.

Mg^{2+} affects the behavior of BMSCs by regulating the phosphorylation of AKT

Mg^{2+} enhanced the proliferation and chondrogenic differentiation and inhibited the osteogenic differentiation of BMSCs by regulating AKT phosphorylation in vitro (Fig. 3A). After treating BMSCs with different concentrations of Mg^{2+} (0, 1, 2, 10, and 20 mM) for 24 hours, there was an increase in the optical density (OD) value at 450 nm, indicating that Mg^{2+} enhanced proliferation of BMSCs (Fig. 3B). However, when the cells were treated for 72 hours, no significant difference was observed, which might be explained by the fact that the confluence of the cells masks the gap. The OD value reached a plateau in the 10 mM group at 24 hours, indicating that 10 mM Mg^{2+} performs best in enhancing proliferation of BMSCs. Moreover, when BMSCs were incubated with gradient concentrations of Mg^{2+} (0, 2, 10, and 20 mM) for 7 and 14 days, the chondrogenic differentiation was significantly enhanced, as suggested by Alcian blue staining. Cartilage nodules became larger, while aggrecan stained with Alcian blue appeared more abundant, and the corresponding quantitation results confirmed the alteration (fig. S3A; Fig. 3, C and D). It should be noted that the relevant quantitative results at 14 days is lower than those at 7 days. Although the Alcian blue staining of BMSCs appeared larger and denser in the Mg^{2+} (14 days) group, it is essential to note that the staining in the control (14 days) group also displayed increased size and density. Consequently, the relative value turned

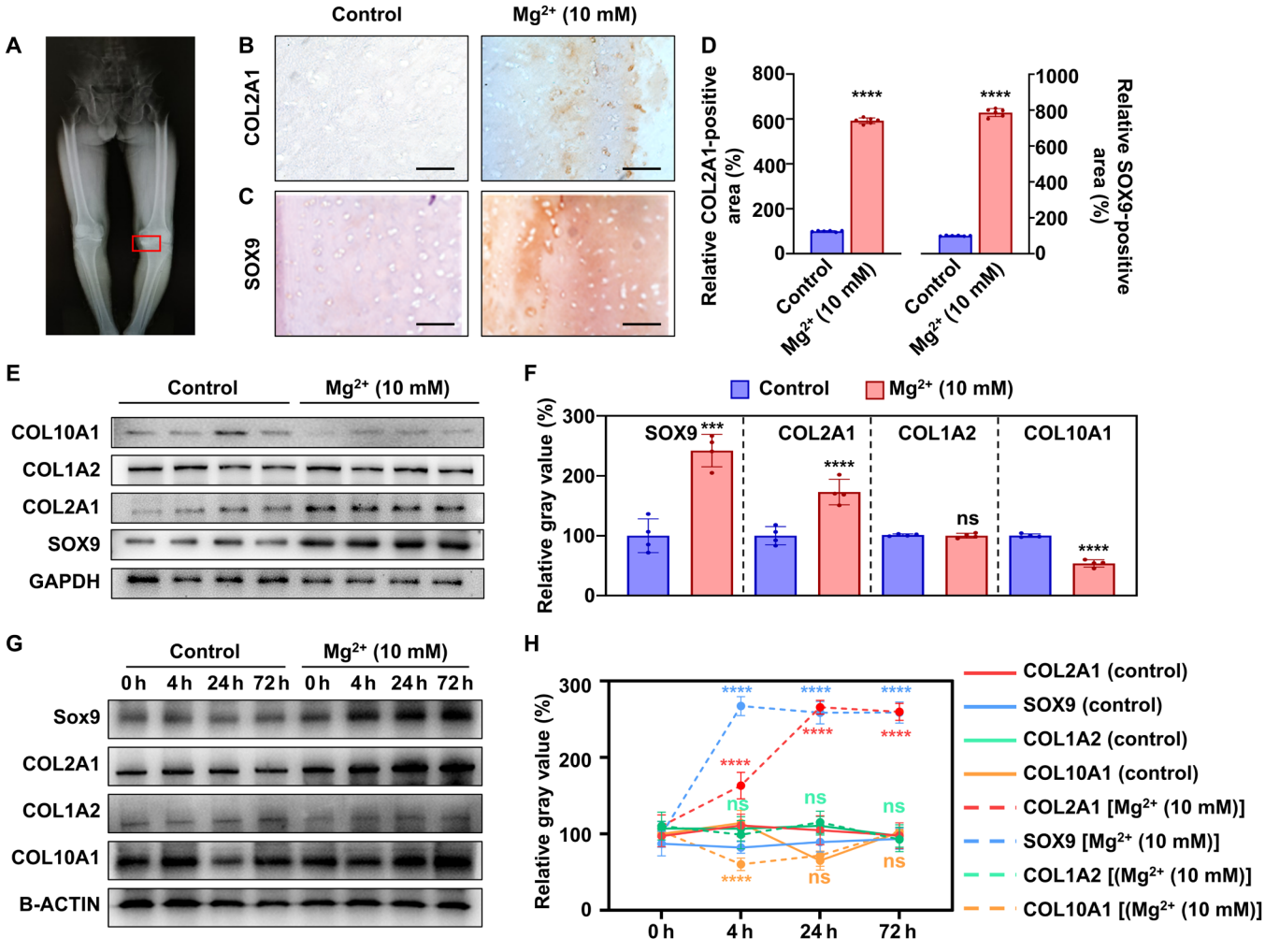

Fig. 2. Mg^{2+} improves chondrocytic phenotype in cartilage tissues from patients with OA. (**A**) A representative radiograph of a patient with OA (patient 3). The red square represents the area of cartilage used for the experiment. Microscopic photographs of COL2A1 (**B**) and SOX9 (**C**) immunostaining in osteoarthritic tissues treated with/without Mg^{2+} (10 mM) for 24 hours, and (**D**) the corresponding quantitative results ($n = 6$). Scale bars, 100 μm. (**E**) Expression of chondrocytic and hypertrophic phenotypic proteins (SOX9, COL1A2, COL2A1, and COL10A1), and (**F**) the corresponding quantitative results ($n = 4$). GAPDH, glyceraldehyde-3-phosphate dehydrogenase. (**G**) Western blot images of SOX9, COL1A2, COL2A1, and COL10A1 isolated from cartilage treated with 10 mM Mg^{2+} for 0, 4, 24, and 72 hours, and (**H**) the corresponding quantitative results ($n = 6$). Notes: All data are shown as the means ± SD. Statistical differences between groups were determined by *t* test and one way analysis of variance (ANOVA). ***$P < 0.001$; ****$P < 0.0001$; not significant (ns) $P > 0.05$.

out to be lower in the Mg^{2+} (14 days) group. This phenomenon indicated that Mg^{2+} accelerated the process of chondrogenic differentiation, while the chondrogenic differentiation reached a plateau in Mg^{2+}-treated group while still at an increasing period in control group in 7 to 14 days.

Notably, the quantitative analysis demonstrated that 10 mM Mg^{2+} had a more pronounced effect on enhancing chondrogenic differentiation compared with other concentrations (fig. S3B). We assessed the chondrogenic protein markers, SOX9 and COL2A1, using Western blot at 7 and 14 days. The expression levels of COL2A1 and SOX9 were the highest when the cells were treated with 10 mM Mg^{2+} (Fig. 3, E and F). These findings indicate that Mg^{2+} (10 mM) promotes chondrogenic differentiation in vitro.

We then evaluate the ability of Mg^{2+} to regulate the osteogenic differentiation of BMSCs. After supplementing the medium with gradient concentrations of Mg^{2+} (0, 1, 10, and 20 mM) for 7 and 28 days, alkaline phosphatase (ALP) staining and alizarin red staining (ARS) revealed a dosage-dependent decline, consistent with the expression of osteogenic-related mRNAs (*RUNX2*, *OPN*, *OCN*, and *COL1A2*) at 7 days (Fig. 3, G to I, and fig. S3, C and D). The relative expression of phosphorylated AKT (P-AKT)/AKT significantly varied among BMSCs treated with different media. In the basic culture medium (BMSCs in a resting state) and chondrogenic differentiation medium, AKT phosphorylation increased significantly in the Mg^{2+}-treated group. However, when BMSCs were treated with osteogenic medium, AKT phosphorylation decreased (Fig. 3, J and K). By further evaluating the underlying pathway, we found that Mg^{2+} activated the INTEGRIN-B1/phosphatidylinositol-4,5-bisphosphate 3-kinase (PI3KCA)/AKT/extracellular signal–regulated kinase (ERK) pathway in the common medium, as revealed by the increased expression of INTEGRIN-B1, PI3KCA, P-AKT, and P-ERK (Fig. 3, L and M).

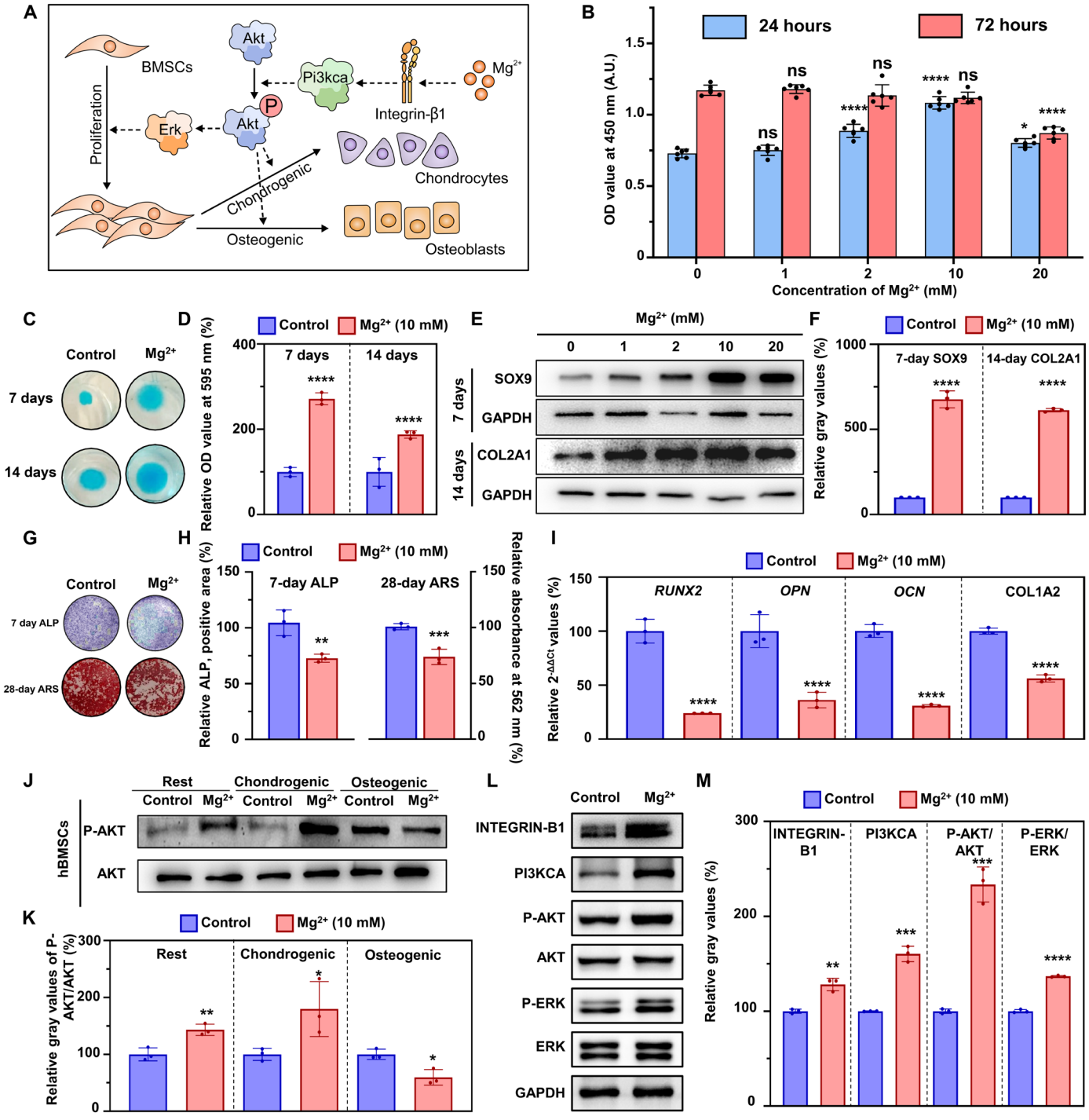

Fig. 3. Mg^{2+} affects the behavior of BMSCs via regulating the phosphorylation of AKT in vitro. (**A**) Schematic illustration showing that Mg^{2+} affects BMSCs' proliferation and chondrogenic and osteogenic differentiation via regulating AKT's phosphorylation in vitro. (**B**) CCK-8 test for BMSCs treated with Mg^{2+} (0, 1, 2, 10, and 20 mM) for 24 and 72 hours ($n = 6$, the comparison was performed between Mg^{2+}-treated groups with the control group). A.U., arbitrary units. (**C**) Photographs of Alcian blue staining of BMSCs after treatment with Mg^{2+} (10 mM) for 7 and 14 days, and (**D**) quantitative results ($n = 3$). (**E**) Protein levels of SOX9 and COL2A1 of BMSCs after treatment with Mg^{2+} (10 mM) for 7 (SOX9) and 14 (COL2A1) days, and (**F**) the quantitative results ($n = 3$). (**G**) ALP (7 days) and ARS (14 days) staining of BMSCs after treatment with Mg^{2+} (10 mM) in osteogenic medium, and (**H**) quantitative results ($n = 3$). (**I**) Relative expression of mRNA (*RUNX2*, *OPN*, *OCN*, and *COL1A2*) of BMSCs after treatment with Mg^{2+} (10 mM) for 7 days ($n = 3$). $2^{-\Delta\Delta Ct}$, delta-delta CT method. (**J**) Protein levels of P-AKT and AKT in BMSCs in common, chondrogenic, and osteogenic medium supplemented with Mg^{2+} (10 mM) for 24 hours, and (**K**) quantitative results ($n = 3$). (**L**) Protein levels of the INTEGRIN-B1/PI3KCA/AKT/ERK pathway of BMSCs cultured in common medium for 4 hours, and (**M**) the quantitative results ($n = 3$). Notes: Scale bars, 100 μm. All data are shown as the means ± SD. Statistical differences between groups were determined by *t* test. $^*P < 0.05$; $^{**}P < 0.01$; $^{***}P < 0.001$; $^{****}P < 0.0001$; ns, $P > 0.05$.

Mg^{2+} inhibits IL-1β–induced chondrocyte apoptosis by activating the PI3K/AKT pathway

Human primary chondrocytes isolated from OA cartilage were used to mimic the inflammation of chondrocytes in OA in vitro. With the supplementation of gradient concentrations of Mg^{2+} (2, 10, and 20 mM), the Alcian blue staining turned darker in color in both inflammatory and noninflammatory environments, which was also verified in the quantitative results (fig. S3, E and F, and Fig. 4, A and B). Simultaneously, the protein levels of COL2A1 and SOX9 increased with the supplementation of Mg^{2+}, while 10 mM Mg^{2+} showed a better phenotype-improving performance compared with 2 and 10 mM groups (Fig. 4, C and D).

Subsequently, interleukin-1β (IL-1β)–treated SW1353 cells were used to mimic inflammatory chondrocytes and investigate the potential mechanism. Treatment with IL-1β (10 ng/ml) significantly increased the apoptosis rate of SW1353 cells, which was reversed by Mg^{2+} (10 mM) supplementation (Fig. 4, E and F). Furthermore, Mg^{2+} treatment led to a significant decrease in the

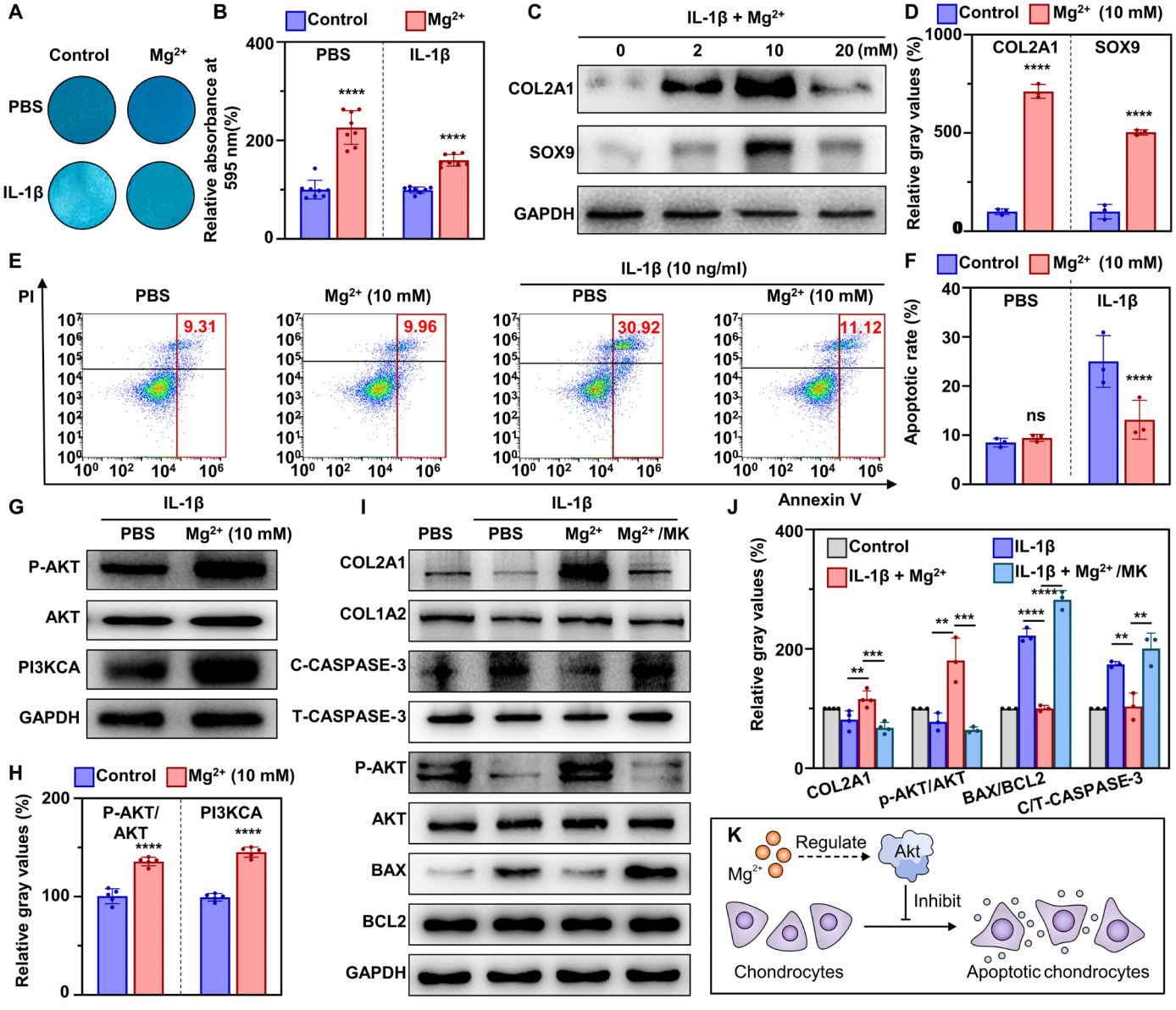

Fig. 4. Mg^{2+} protects chondrocytes from inflammation-induced apoptosis via activating the AKT–CASPASE-3 pathway in vitro. (**A**) Alcian blue staining of primary human chondrocytes after culture in conditioned medium for 24 hours, and (**B**) the corresponding quantitative results ($n = 8$). (**C**) Western blot images of COL2A1 and SOX9 of primary human chondrocytes after culture in conditioned medium for 24 hours, and (**D**) the corresponding quantitative results ($n = 8$). (**E**) Cell apoptosis level of SW1353 cells after culture in conditioned medium for 24 hours, and (**F**) the corresponding quantitative results ($n = 3$). (**G**) Protein levels of phosphorylated AKT and PI3KCA after treatment with Mg^{2+} (10 mM), and (**H**) the corresponding quantitative results ($n = 5$). (**I**) Key protein levels of the apoptosis-related AKT–CASPASE-3 pathway in SW1353 chondrocyte cell line after treatment with conditioned medium for 24 hours, and (**J**) the corresponding quantitative results ($n = 3$). (**K**) Schematic illustration of the process by which Mg^{2+} inhibits chondrocytes apoptosis via regulating the AKT–CASPASE-3 pathway. Notes: All data are shown as the means ± SD. Statistical differences between groups were determined by *t* test. $^{**}P < 0.01$; $^{***}P < 0.001$; $^{****}P < 0.0001$; ns, $P > 0.05$.

apoptosis-related genes CASPASE-3, CASPASE-8, CASPASE-9, and BAX/BCL2 relative to the control group (fig. S4A). Upstream proteins, including PI3KCA p110α and P-AKT, exhibited a significant increase after treatment with Mg^{2+} (Fig. 4, G and H). To examine the role of AKT in the antiapoptotic effect of Mg^{2+}, chondrocytes incubated with Mg^{2+} were treated with MK2206, an AKT inhibitor. Upon Mg^{2+} treatment, AKT phosphorylation was activated, leading to a significant decrease in the apoptotic markers cleaved CASPASE-3 and BAX/BCL2 at the protein level (Fig. 4, I and J). However, supplementation with MK2206 resulted in a significant decrease in P-AKT and chondrocytic markers (COL2A1 and SOX9), while apoptotic markers (CASPASE-3, CASPASE-8, CASPASE-9, and BAX/BCL2) increased at both mRNA and protein levels (fig. S4B). These findings indicated the importance of AKT phosphorylation in the antiapoptotic effect of Mg^{2+} via the PI3K/AKT pathway. Collectively, these results demonstrate that Mg^{2+} (10 mM) protects chondrocytes from inflammatory damage by inhibiting apoptosis through the PI3K/AKT pathway (Fig. 4K).

Mg^{2+} inhibits the formation and function of osteoclasts via inhibiting AKT phosphorylation

As shown in tartrate-resistant acid phosphatase (TRAP) and immunostaining analysis, both the area and the number of osteoclasts exhibited a significant decrease, indicating the inhibition of osteoclast formation (Fig. 5, A to C). Subsequently, calf bone slices seeded with osteoclasts were used to assess their bone resorptive function. As shown in scanning electron microscopy (SEM) images, the newly formed bone resorptive lacunas were no longer observed following the treatment with 10 mM Mg^{2+} (Fig. 5D), suggesting the inhibition of osteoclast function. Moreover, the phosphorylation level of AKT in osteoclasts showed a significant decrease (Fig. 5, E and F), which was closely associated with osteoclast survival. We also used transcriptome sequencing to analyze the differences in genes and found that, among the up-regulated genes, the PI3K/AKT pathway accounted for the most significant alteration in addition to proteoglycans and focal adhesion (Fig. 5, G and H). Collectively, our findings demonstrate that Mg^{2+} effectively inhibits the formation and function of osteoclasts by suppressing AKT phosphorylation.

MPs were successfully prepared and characterized

To enhance the dispersibility of MgO nanoparticles in PLGA solution, we used biocompatible stearic acid (SA) molecules to modify the MgO nanoparticles. The modification aimed to improve the loading efficiency of the nanoparticles within the PLGA MPs (Fig. 6A). During the preparation of MgO&SA@PLGA, neither anhydrous ethanol nor dichloromethane (DCM) can destroy MgO nanoparticles and release Mg^{2+} when used as solvents. Even during the solvent evaporation process, there is no significant release of Mg^{2+} because MgO&SA is modified through a hydrophobic interaction over a short period. Our previous studies have demonstrated that the utilization of fatty acids for the modification of $Mg(OH)_2$ or MgO can enhance the interaction between the inorganic interface and fat-soluble polymers such as PLGA and poly(trimethylene carbonate) (PTMC) (*13*). X-ray diffraction (XRD) patterns and transmission electron microscopy (TEM) images revealed that treatment with SA did not affect the structure and size of the MgO nanoparticles (Fig. 6B and figs. S5 and S6).

To investigate the anchoring of SA molecules on the surface of MgO, Fourier-transform infrared spectroscopy (FTIR) analysis was conducted. The FTIR spectrum of MgO&SA, as shown in fig. S7, exhibited characteristic peaks at ~2973 cm^{-1} for $-CH_3$ groups and 2883 cm^{-1} for $-CH_2$ groups, which were similar to those of SA. This finding confirmed the successful modification of the MgO surface by SA molecules. Furthermore, the hydrophobic properties of MgO&SA tablets were examined (Fig. 6C). While MgO displayed a superhydrophilic nature, the surface of MgO&SA exhibited hydrophobicity, with an average contact angle (CA) even greater than 136°. This hydrophobicity may be explained by the presence of $-CH_3$ groups at the end of SA molecules.

To enhance the dispersibility of MgO&SA nanoparticles in DCM compared with MgO, we introduced different nanoparticles into a DCM solution and performed ultrasonic treatment. After centrifugation, we found clear precipitation of MgO in the MgO group, while there was a little precipitation in the MgO&SA group (Fig. 6D). Dynamic light scattering (DLS) results demonstrated that MgO&SA (30) exhibited the narrowest size distribution, ~100 nm in DCM. Both MgO&SA (7.5) and MgO&SA (30) showed aggregation in DCM, which was attributed to incomplete modification and excessive fatty acids, respectively (fig. S8). Therefore, we selected MgO&SA (30), referred to as MgO&SA nanoparticles, for loading into PLGA microspheres for subsequent experiments.

Compared with PLGA microspheres, the MPs exhibited a broader size distribution ranging from 3.36 ± 1.79 μm to 3.72 ± 1.93 μm (fig. S9). The surface of MPs displayed small holes, possibly due to residual SA molecules or loss of MgO&SA nanoparticles (Fig. 6E). To confirm successful encapsulation of MgO&SA nanoparticles within PLGA microspheres, energy-dispersive x-ray spectroscopy (EDS) mapping was used, revealing an even distribution of Mg elements within the MPs (Fig. 6E). In addition, we explored the loading efficiency of MgO particles in the PLGA microspheres by analyzing the content of Mg in the liquid supernatant. The loading efficiency is calculated as 65.90% subsequently.

The degradation behavior was evaluated by monitoring the pH variation and Mg^{2+} release. In vitro immersion testing in phosphate-buffered saline (PBS) at 37 ± 0.5°C for up to 14 days was used to assess the degradation rate. The degradation reaction for MgO-based materials can be represented as follows: $MgO + H_2O \rightarrow Mg^{2+} + 2OH^-$. This indicates that the generation of 1 mol Mg^{2+} consumes 1 mol MgO while producing 2 mol OH^-. Initially, the pH change in the immersion solution was monitored over time. The MgO group exhibited more significant pH value changes than all other groups, particularly during the early stage (~4 days). In contrast, the pH value of the PLGA group steadily decreased to around 7.0, indicating the formation of acidic products. The MP group maintained a stable pH in the long term due to the preventive effect of PLGA on MgO degradation, and the degradation products of PLGA, such as lactic acid, contributed to pH regulation by neutralizing the OH^- released from MgO degradation. As a bioactive element involved in the regulation of chondrogenesis, the Mg^{2+} concentration mirrored the pH evolution (Fig. 6F). The Mg^{2+} concentration reached significantly higher levels early on and maintained this state in the later stage, surpassing that of the MP group. The MPs achieved controlled Mg^{2+} release with a smooth release rate over 14 days (Fig. 6G). In addition, conspicuous magnesium phosphate crystals were found in the later stage of the MgO group, attributable to the higher concentration of Mg^{2+} precipitating as crystals.

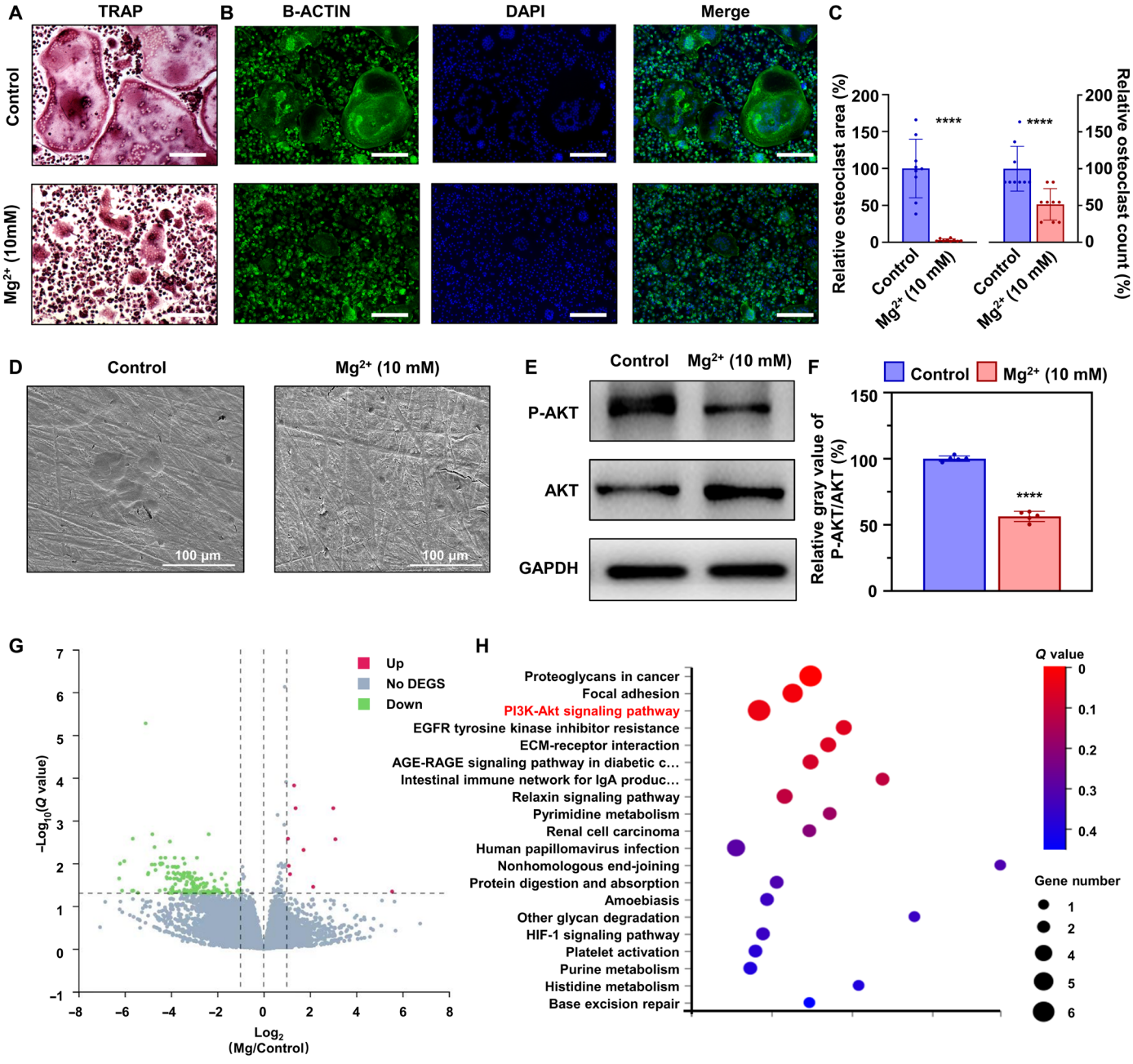

Fig. 5. Mg^{2+} inhibits the formation and function of osteoclasts via inhibiting the phosphorylation of AKT in vitro. (**A**) TRAP and (**B**) immunofluorescence (Actin-belt) staining of BMMs after treatment with osteoclastic medium with/without Mg^{2+} (10 mM) for 7 days, and (**C**) the corresponding quantitative results ($n = 9$). Scale bars, 200 μm. (**D**) SEM images of bone slices seeded by BMMs after treatment with osteoclastic medium with/without Mg^{2+} (10 mM) for 7 days. Scale bars, 100 μm. (**E**) Protein levels of P-AKT and AKT in BMMs treated with osteoclastic medium with/without Mg^{2+} (10 mM) for 7 days, and (**F**) the corresponding quantitative results ($n = 6$). (**G** and **H**) Differentially expressed genes (DEGs) and the Kyoto Encyclopedia of Genes and Genomes pathway analysis of Mg^{2+}-treated BMMs. ECM, extracellular matrix; EGFR, epidermal growth factor receptor; HIF-1, hypoxia-inducible factor1; IgA, immunoglobulin A; AGE-RAGE, advanced glycation endproducts-the Receptor of Advanced Glycation Endproducts. Notes: All data are shown as the means ± SD. Statistical differences between groups were determined by *t* test. ****$P < 0.0001$.

MPs protect rats from instability-induced OA

After characterization in vitro, the MPs were injected into the articular cavities of OA rats to evaluate the in vivo effects. The therapeutic effect on OA was reflected in the alterations in gait and pain of the examined rats. Therefore, we performed gait analysis and the Von Frey pain test. As shown in Fig. 7A, spatial asymmetry was calculated on the basis of the distribution of left and right gaits. In the control group, the red-marked right front and hind tracks did not overlap with the blue-marked tracks at 2- and 4-week time points after medial meniscus tear (MMT) surgery, indicating spatial asymmetry (Fig. 7B). However, with MP treatment, the tracks overlapped, and the stride length became more extended compared

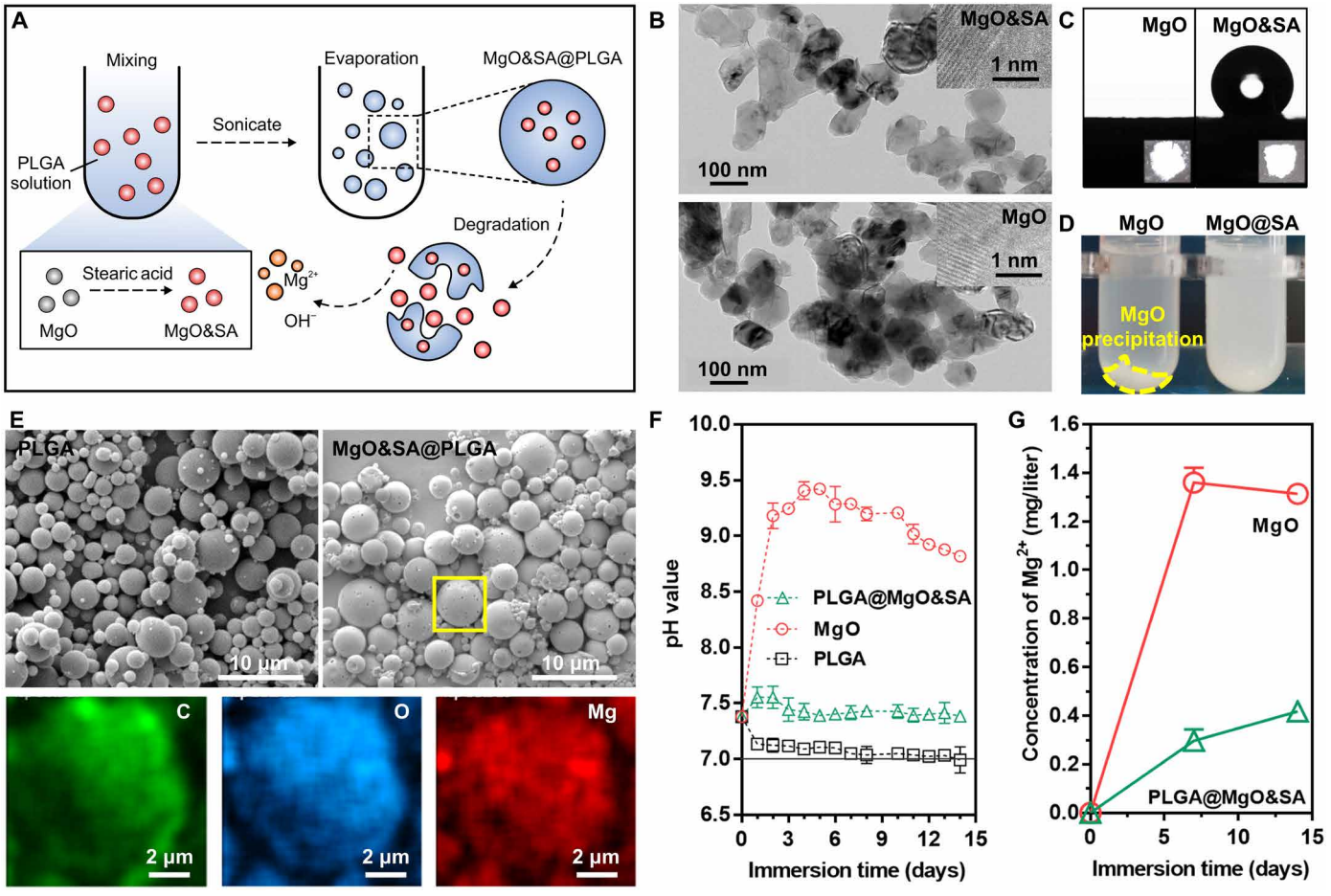

Fig. 6. Preparation and characterization of engineered MgO&SA@PLGA microspheres. (**A**) Schematic diagram of the preparation of engineered MgO&SA@PLGA microspheres. (**B**) Transmission electron microscopy (TEM) images. (**C**) Water contact angle (CA). (**D**) Dispersibility of MgO nanoparticles after treatment with SA. (**E**) SEM images and EDS mapping (corresponding to the yellow box of MgO&SA@PLGA). (**F**) pH value change and (**G**) Mg^{2+} release in PBS at 37 ± 0.5°C as a function of time (14 days).

with that in the control group. In addition, the hindlimb footprint of the rats in the MP group was approximately halfway between the two left hindlimb footprints. Quantitative results demonstrated that spatial stability tended to be lost in the control group but recovered in the MP group (Fig. 7C). In the pain test, the pain threshold significantly decreased in the control group compared with the sham group, indicating a more sensitive reaction to pain stimuli. Conversely, with MP treatment, the pain threshold increased significantly at 2- and 4-week time points after MMT surgery (Fig. 7D). These results indicate that MPs effectively relieve pain symptoms in OA rats.

Four weeks after destabilizing medial meniscus surgery (Fig. 8A), the rats treated with saline exhibited an apparent cartilage defect. In contrast, we found a smoother cartilage surface in the MP-treated group (Fig. 8B). Representative microscopy images of the joint tissue sections stained with Safranin O/Fast Green revealed apparent cartilage defects and osteophytes in the control group, while fibrillation was observed in the MP group (Fig. 8C). In addition, immunostaining of COL2A1 indicated that the newly formed cartilage was natural hyaline cartilage (Fig. 8D). Micro–computed tomography (micro-CT) analysis revealed the presence of newly formed osteophytes around the knee in the control group, whereas the MP group showed almost no osteophyte formation in 4 weeks (Fig. 8E). The degrees of cartilage degradation, osteophyte formation, calcified cartilage, subchondral bone damage, and synovial membrane inflammation were individually evaluated on the basis of the Osteoarthritis Research Society International (OARSI) system (Fig. 8F). There was a significant decrease in the MP group, indicating milder joint cartilage damage compared with the control group (Fig. 8G). Terminal deoxynucleotidyl transferase–mediated deoxyuridine triphosphate nick end labeling staining was performed on sections with continuous cartilage surfaces in the edge of the lesion area (Fig. 8H). In the control group, the positive cell rate was 25.31 ± 7.83 times higher than that in the sham group. However, with MP treatment, the rate decreased to the average level of the sham group (Fig. 8I). These results demonstrate that MPs protect the cartilage in OA rats from damage by inhibiting chondrocyte apoptosis in vivo.

MPs protect the subchondral bone from instability-induced OA

As shown by Safranin O/Fast Green staining of the knee sections, there was a large subchondral bone cyst beneath the medial tibial

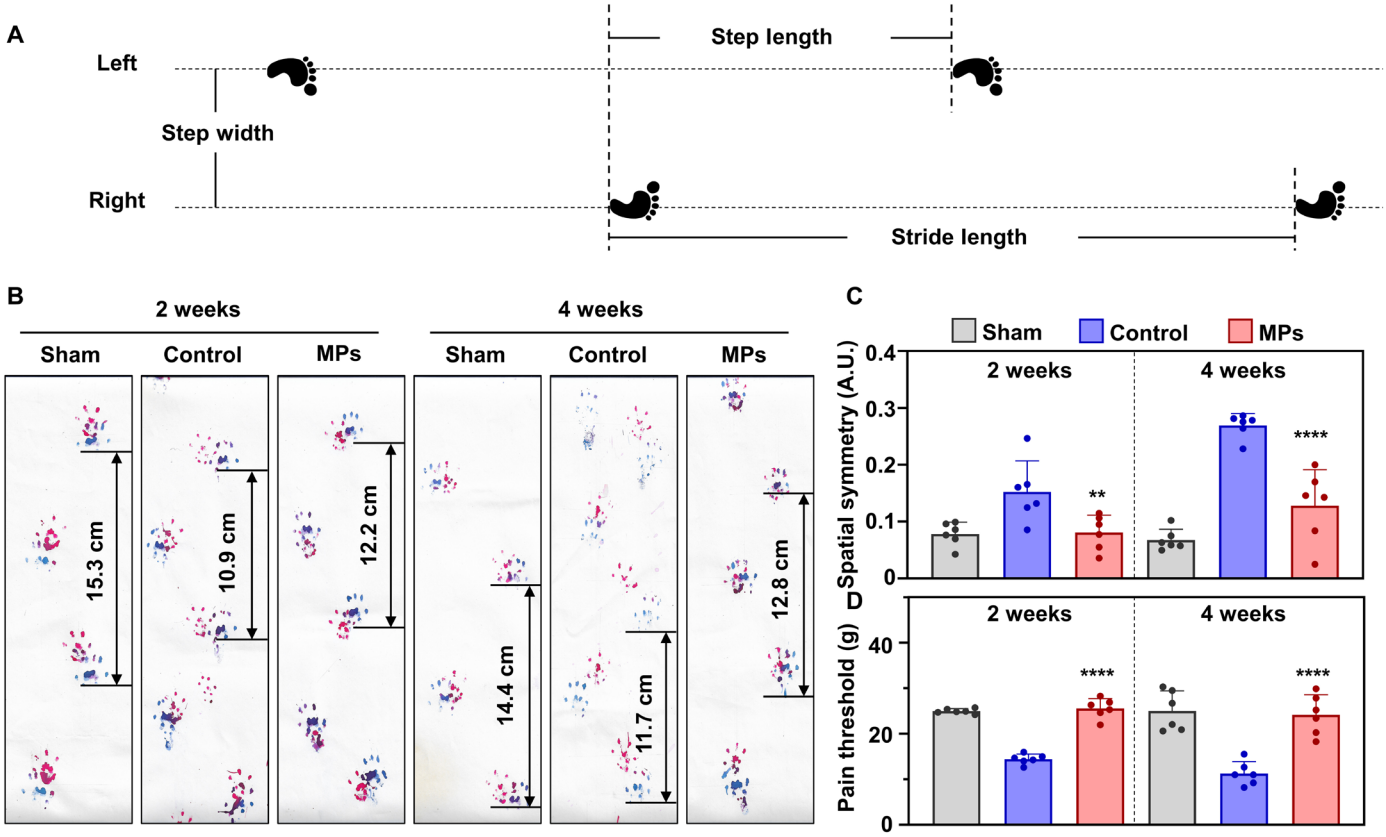

Fig. 7. Mg^{2+}-releasing MPs relieve pain and gait in a rat OA model. (**A**) Schematic diagram of measurement indexes for gait analysis. (**B**) A photograph of the rats' gait after conditional treatment for 2 and 4 weeks. (**C**) Spatial symmetry calculation results of the rats after conditional treatment for 2 and 4 weeks ($n = 6$). (**D**) Pain threshold of the rats tested at 2 and 4 weeks after conditional treatment ($n = 6$). Notes: All data are shown as the means ± SD. Statistical differences between groups were determined by one-way ANOVA. $^{**}P < 0.01$; $^{****}P < 0.0001$.

plateau, occupying almost all subchondral bone areas in the control group. However, this was not the case in the MP-treated groups (Fig. 8C). On the basis of this, the subchondral bone ranging from the osteo-epiphysis to the joint surface (Fig. 9A) was selected for the analysis of bone morphological parameters. Consistent with the section photographs, a significant bone cyst was observed in the control group, while it disappeared in the MP group (Fig. 9B). We found a significant decrease in bone mineral density (BMD) of total volume (TV) in the OA rats, whereas MP treatment increased BMD of TV to the level of the sham group. Specifically, bone volume (BV) fraction (BV/TV), instead of BMD of BV, showed a clear alteration (Fig. 9, C to E). The micro-CT results showed that MPs protected the subchondral bone damage caused by OA. Other bone morphological parameters are presented in table S2. Furthermore, the bone turnover level was assessed in vivo. The TRAP staining revealed a decrease in the TRAP-positive erosive area (Er.Pm) in both subchondral and cancellous bone with MP treatment, indicating the decrease in bone resorption activity (Fig. 9, F to H). Moreover, Masson staining demonstrated a significant increase in newly formed osteoid (quantified as O.Pm) in the two areas, indicating the increased bone formation in vivo. Calcein and xylenol orange staining of newly formed osteoid at 2 and 3 weeks revealed that the bone formation rate (BFR) increased in both the control and the MP groups compared with the sham group, with a higher value observed in the MP group (2.707 ± 0.421 μm/day) than in the control group (1.735 ± 0.035 μm/day). This was supported by the results of Masson staining that demonstrated the increased bone formation level in the subchondral bone (Fig. 9, L and M). These findings suggest that the MPs protect the subchondral bone in rats from OA damage in vivo.

MPs are biosafe in vivo

Four weeks after MP injection, we evaluated their biocompatibility. Experienced pathologists examined hematoxylin and eosin (H&E)–stained sections of crucial metabolic organs, such as the hearts, livers, kidneys, and lungs. No structural differences or signs of inflammatory cell infiltration were found (fig. S10). Furthermore, we analyzed serum biochemical markers of hepatic and renal functions, namely, alanine aminotransferase (ALT), aspartate aminotransferase (AST), blood urea nitrogen (BUN), and creatinine (Cr), and found no indications of damage (fig. S11, A to D). We also assessed the levels of serum Ca^{2+} and Mg^{2+} and found no abnormalities (fig. S11, E and F).

DISCUSSION

Mg^{2+} is the fourth most common divalent cation in the human body and the second most abundant intracellular cation, and it is primarily stored in the skeletal system (*24*). Considering the excellent bioactivity

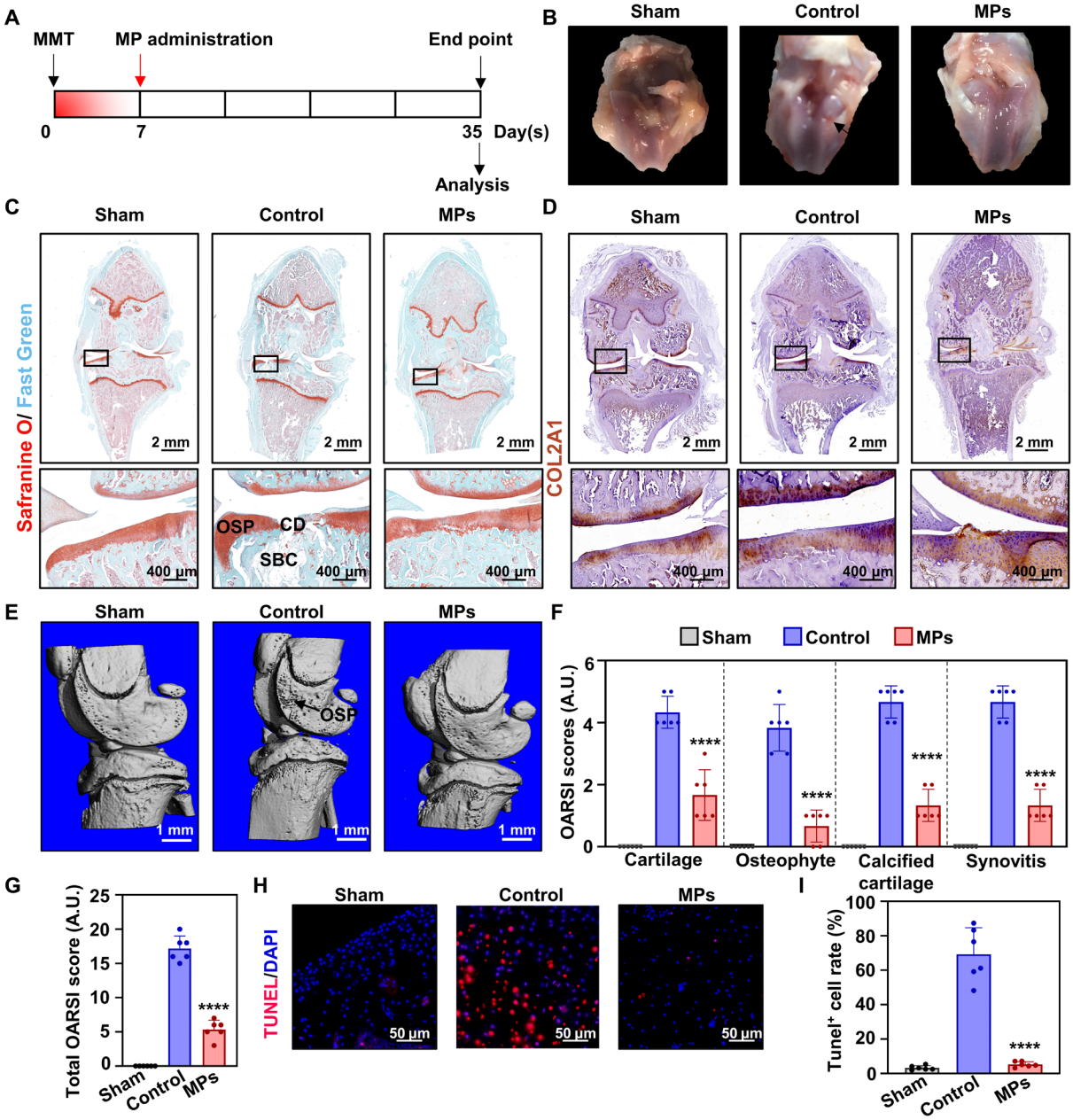

Fig. 8. Mg^{2+}-releasing MPs protect cartilage in a rat OA model. (**A**) Timeline of the animal experiments. The MPs were administered to the rats' joint cavity 7 days after the MMT surgery, and another 28 days were used for the treatment of OA. (**B**) Representative photographs of the rats' knee cartilage after conditional treatment. The black arrow refers to the obvious cartilage defect. (**C**) Representative microscopic photographs of Safranine O/Fast Green staining. The areas in the black squares are magnified and shown separately. OSP, osteophytes; CD, cartilage defect; SBC, subchondral bone cyst. Scale bars, 2 mm and 400 μm. (**D**) Immunostaining of COL2A1 in the rats' knee cartilage sections. Scale bars, 2 mm and 400 μm. (**E**) Three-dimensional (3D) reconstruction of micro-CT results of the rats' knees. The black arrow refers to the osteophytes. Scale bars, 1 mm. (**F**) OARSI score of cartilage, osteophyte, calcified cartilage, and synovitis ($n = 6$). (**G**) Total OARSI score in different groups ($n = 6$). (**H**) Representative microscopic photographs of terminal deoxynucleotidyl transferase–mediated deoxyuridine triphosphate nick end labeling (TUNEL) staining of the rats' knee sections. Red fluorescence represents apoptotic cells, and blue fluorescence represents cellular nuclei. Scale bars, 50 μm. DAPI, 4′,6-diamidino-2-phenylindole. (**I**) Quantitative results of TUNEL staining ($n = 6$). Notes: All data are shown as the means ± SD. Statistical differences between groups were determined by one-way ANOVA. ****$P < 0.0001$.

and biodegradability, Mg-based biomaterials have widely been applied in the bone and cartilage tissue engineering, while Mg^{2+}-enriched hyaluronic acid has been approved in Europe for cartilage repair (*10*, *25*, *26*). Previous epidemiological studies have demonstrated a significant decrease in systemic and local levels of Mg^{2+} in patients with OA, which is positively associated with knee deterioration and structural damage (*27*, *28*). As shown in animal experiments, supplementation with Mg^{2+} effectively protects the knee joint from OA damage (*20*). Although the therapeutic effect has previously been explained by the alleviation of inflammation and the inhibition of apoptosis, the mechanistic explanations focused on one kind of tissue instead overall joint. It has been noted that Mg^{2+} might enhance

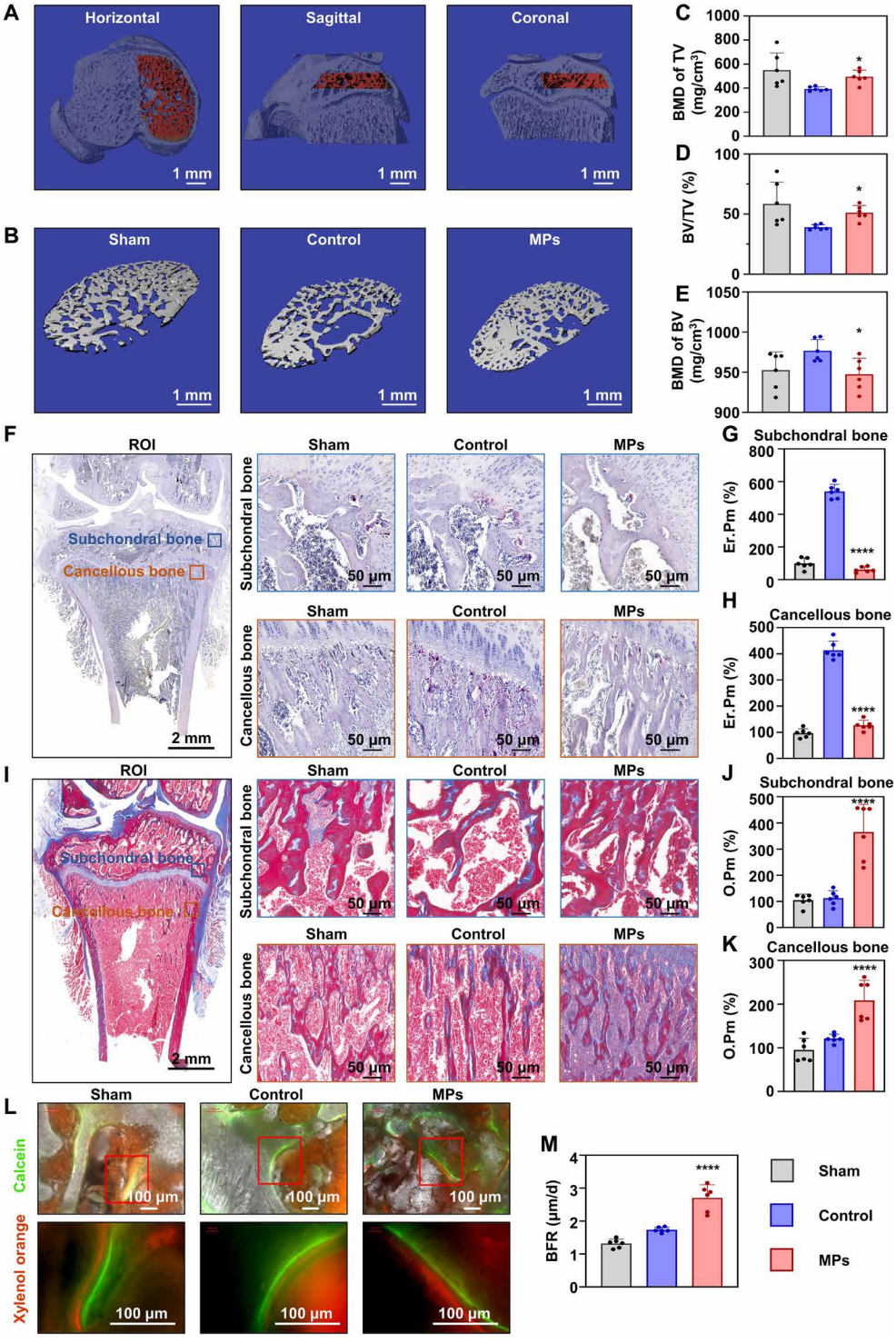

Fig. 9. Mg^{2+}-releasing MPs improve subchondral bone in a rat OA model. (**A**) Three views of the region of interest (ROI) selected for analysis of the subchondral bone. Scale bars, 1 mm. (**B**) 3D reconstruction of subchondral bone after conditional treatment for 4 weeks. Scale bars, 1 mm. Quantitative results of bone mineral density (BMD) of total volume (TV) (**C**), BV fraction (BV/TV) (**D**), and BMD of BV (**E**) of subchondral bone ($n = 6$). (**F**) TRAP staining of tibia. The Er.Pm of (**G**) subchondral ($n = 6$) and (**H**) cancellous bone ($n = 6$). Scale bars, 1 mm and 50 μm. (**I**) Masson trichrome staining of tibia. The O.Pm of (**J**) subchondral ($n = 6$) and (**K**) cancellous bone ($n = 6$). Scale bars, 1 mm and 50 μm. (**L**) Calcein- and xylenol orange–marked subchondral bone after conditional treatment for 2 and 3 weeks, and (**M**) the bone formation rate (BFR; $n = 6$). Scale bars: 100 μm. Notes: All data are shown as the means ± SD. Statistical differences between groups were determined using the Kruskal-Wallis test due to the difference in variance. $^{*}P < 0.05$; $^{****}P < 0.0001$.

the cell adherence, migration velocity and proliferation, and chondrogenic differentiation, but experimental evidence is still needed (*29*). Our current studies have provided compelling evidence that Mg^{2+} can enhance chondrogenic differentiation and inhibit chondrocyte apoptosis. Furthermore, the therapeutic effect may be partially attributed to its regulation of bone metabolism. Combined with our previous findings that Mg^{2+} can effectively alleviate synovitis, we believe that Mg^{2+} has the potential to become a promising next-generation anti-OA therapeutic drug, which simultaneously regulates multiple periarticular tissues (*21*). The present work also provided strong experimental evidence for the preparation of Mg^{2+}-containing vehicles for treating OA.

To elucidate the anti-OA effect of Mg^{2+}, we examined the distinct effects of Mg^{2+} on the regulation of AKT phosphorylation in different cell types. The role of P-AKT in OA has generated controversy in previous studies (*30*). On the one hand, the activation of the PI3K/AKT pathway can enhance extracellular matrix anabolism, promote chondrocyte proliferation, and inhibit apoptosis. In our experiments, we used some key proteins, such as ERK and CASPASE-3, as examples to evaluate the function of AKT phosphorylation. We used the sample to prove that the regulation of proliferation is of significance. In other processes, factors other than ERK might play an important role, such as the AKT–CASPASE-3 pathway in the regulation of cellular apoptosis. In this work, we focused more on the regulatory effect of Mg^{2+} on the AKT protein, while the determined pathway should be explored in the future works. The phosphorylation of AKT is also linked with cartilage catabolism and subchondral bone sclerosis. Here, we cultured OA cartilage tissues encompassing both catabolic and anabolic processes from patients with OA. We discovered that Mg^{2+} concurrently up-regulated representative catabolic factors and anabolic markers (COL2A1 and SOX9), suggesting a state of heightened metabolic equilibrium within the cartilage. Another aspect concerns subchondral bone sclerosis, which is conceptually ambiguous. Previous investigations have shown that early-stage OA typically exhibits reduced bone density, while the subchondral cancellous bone beneath the subchondral plate may remain osteopenic (*31*, *32*). According to previous work (*33*), our data indicated that OA in the MP group of rats was in the early stage, whereas OA in the control group was in the advanced stage. However, the BFR of our sham control was higher than 0.7 μm/day but still lower than 1.4 μm/day, which may be attributed to differences between animal species. This phenomenon can be attributed to the differential regulatory effects of Mg^{2+} across various cell types, which ultimately prove advantageous for OA treatment (*34*). Consequently, we termed this therapeutic effect the "bone-cartilage synergistic effect."

Protein phosphorylation is a crucial posttranslational modification process. Through an extensive review of the literature, we concluded that this phenomenon could potentially be explained by the enzymes involved in phosphorylation in various cell types. Calcium- and calmodulin-dependent protein kinases (CaMKs), particularly CaMKII, are activated by Ca^{2+} but are often competitively inhibited by Mg^{2+}. CaMKII facilitates the reaction between adenosine 5′-triphosphate and Ser, resulting in the production of H^+. In osteoclasts, the acidic microenvironment is more conducive to this reaction, and the addition of Mg^{2+} may inhibit AKT phosphorylation by suppressing CaMKs activity (*35*–*37*). In contrast, in BMSCs, the neutral or alkaline microenvironment favors the activity of protein phosphatase 2s (PP2s), an Mg^{2+}-dependent protein phosphatase (*38*–*40*). The addition of Mg^{2+} may enhance AKT phosphorylation by activating the PP2s activity. Briefly, the bone-cartilage synergistic effect is based on the balance of Mg^{2+} and Ca^{2+}. These assumptions need to be explored further in the future.

To deliver Mg^{2+} into the joint cavity, we first need to identify a suitable Mg^{2+} provider. It is known that metallic Mg has the highest Mg content, but their high reactivity makes them easily released in the joint cavity filled with joint fluid, rendering them unsuitable for clinical translation due to biosafety concerns (*41*). In contrast, $MgCO_3$ and $Mg(OH)_2$ are more stable, but their Mg content is lower than that of MgO. In addition, ionic compounds such as $MgCl_2$, $MgSO_4$, and magnesium gluconate can be directly injected into the joint cavity, but it is challenging to prepare them as sustained-release drugs. Therefore, MgO was ultimately chosen as the Mg^{2+} provider in this study. In previous studies focusing on bone defect regeneration, surface-modified MgO coated with the Food and Drug Administration (FDA)–approved polymer vehicle PLGA was used (*42*, *43*). The degradation of PLGA generates an acidic environment capable of neutralizing the alkaline environment produced by MgO. To increase the loading rate and Mg^{2+} content, we modified the MgO using SA and prepared microspheres measuring 2 to 3 μm in size. The use of SA molecules to modify MgO nanoparticles improves the dispersity of nanoparticles in preparation of MgO&SA@PLGA. In our previous work (*13*), SA molecules were used to pretreat $Mg(OH)_2$ coating to reduce the gap below a poly(1,3-trimethylene carbonate) (PTMC) layer, which improved the adhesion strength and anticorrosion behavior. Meanwhile, the pH changes of AZ31-OH&SA@PTMC remained around 7.7 ± 0.1, which benefited from the SA molecules' modification of the surface of MgO and $Mg(OH)_2$. The present work chose a similar strategy in the nanoscale, which not only increases the loading efficiency of MgO but also regulates Mg^{2+} sustained release. In addition, the MPs used in our study were prepared using FDA-approved PLGA as the base material for drug delivery.

In our animal experiments, a single injection was administered instead of repeated injections of Mg^{2+}, and a similar protective effect was demonstrated. However, we noticed the appearance of cartilage fibrosis in the group treated with MPs, suggesting that degradation in vivo differs from the in vitro situation. According to clinical results, supplementation of Mg^{2+} in the joint cavity reduces pain as assessed by the von Frey test (*44*). Overall, the MPs demonstrated a satisfactory therapeutic effect in animal models and are promising for the clinical translation. The treatment view of OA has shifted toward the systemic treatment, which includes three stages: lifestyle changes, drugs, and surgical operation. On the basis of our results, we believe that the Mg-based therapy could be translated to clinical application in the first two stages: the nutritional intervention and intra-articular injection. In the patients with the risk factors for OA, such as those with obesity and knee trauma, the dietary supplementation of Mg^{2+} should be encouraged. When there is radiological evidence of early OA, such as the signal change in cartilage and subchondral bone area in magnetic resonance imaging, our agents could be applied by the intra-articular puncture. In addition, in the patients with inaccurate low limb alignment, the combination of high tibial osteotomy and distal femoral ostomy operation with the agents might promote the stimulation of cartilage regeneration. By incorporating MgO&SA, the acidic degradable products were rendered neutral, making them more suitable for drug loading purposes. a single injection of MgO&SA@PLGA could provide a sustained release of Mg^{2+} in microenvironments, which could avoid repeated injections of Mg^{2+}. Treatment with multiple injections of Mg^{2+} has

been reported previously (*20*), and our strategy using MgO&SA@PLGA aimed to improve the compliance of patients.

There were some limitations to this study. First, the material design may be further improved. The therapeutic effect might be enhanced by co-loading other well-recognized drugs that target different aspects of OA. For example, loading of kartogenin or other bioactive molecules stimulates the regeneration of cartilage, and parathyroid hormone enhances the protection of subchondral bone (*45*–*47*). However, in terms of future translational work, the simplest formula is highly recommended, and the MPs are promising as a foundation for developing multifunctional microvehicles. Second, we did not explain how Mg^{2+} affects the phosphorylation of AKT in different cells. Although we hypothesized that the different acid-base microenvironment in different cells plays an important role in the process, it is hard to verify the synergistic effect in vivo due to the complex microenvironment and multiple kinds of cells involved in the process of OA. The problem might be solved with the combination of stem-cell tracing, single-cell sequencing, and spatial transcriptomics. The Mg^{2+} concentration in synovial fluid directly affects treatment effectiveness, while the volume of synovial fluid in rats' joint cavities is too small for quantitative analyses. As shown in fig. S1 (A to C), the Mg^{2+} concentration not higher than 20 mM is safe in both inflammatory and noninflammatory environments. In this work, the total volume of MgO injected in the joint cavity was 164.74 μg, which was eight times that of the in vitro studies. The sustainable release of Mg^{2+} may have resulted in the period when Mg^{2+} was at its effective concentration being less than 1 month. In this work, we found that the rats in the MP group were still in the early stage of OA, which might result in an underestimation of the therapeutic effect of Mg^{2+}. Further studies are needed to verify these findings and improve treatment outcomes.

To conclude, Mg^{2+} can protect both cartilage and subchondral bone in cases of OA, and the combined effect on these tissues can explain the therapeutic benefits through the activation of the PI3K/AKT pathway, both in vitro and in vivo. To enhance the therapeutic effect, we developed and fabricated MPs, enabling the targeted delivery of Mg^{2+} into the joint cavity. The MPs demonstrated satisfactory therapeutic efficacy and exhibited excellent biocompatibility in vivo, providing further evidence for the synergistic effect of Mg^{2+} in treating OA-related issues in both cartilage and subchondral bone.

MATERIALS AND METHODS

Materials and characterization

MgO, SA, absolute ethanol, DCM, and Vitamin E Polyethylene Glycol Succinate (TPGS) were purchased from Shanghai Aladdin Biochemical Technology Co. Ltd. PLGA (LA/GA, 50:50; molecular weight, 150,000) was obtained from Jinan Daigang Biotechnology Co. Ltd. All reagents were used as received without further purification. All aqueous solutions used in the experiments were prepared using deionized water (18.2 megaohms·cm, Millipore).

Preparation of MgO&SA nanoparticles

First, MgO nanoparticle powders were purchased from Aladdin Biochemical Technology Co. Ltd. and placed in a 160°C oven for 2 hours to eliminate excess water. Next, MgO nanoparticles (300 mg) were dispersed in absolute ethanol (100 ml) and sonicated for 10 min. SA (7.5, 15, 30, or 60 mg) was added to the MgO nanoparticle solution while stirring and refluxed for 12 hours. Then, the resulting SA-modified MgO nanoparticles were centrifuged and subjected to three rounds of cleaning. Last, the SA-modified MgO nanoparticles were treated at 120°C for deprotonation and designated as MgO&SA.

Preparation of MgO&SA@PLGA microspheres

The choice of the dosage was based on our in vitro studies, the encapsulation efficiency, and the release profile data. In the in vitro studies, we considered 10 mM Mg^{2+} as suitable for the treatment of OA. Considering that the joint cavity was about 50 μl, the total amount of Mg^{2+} was 500 nmol (10 nmol/μl × 50 μl). The mass of MgO used was 20 μg (500 nmol × 40 ng/nmol). Given that the sustainable-releasing system cannot release all Mg^{2+} immediately after injection and that the metabolism in vivo is faster than that in vitro, we increased the dosage of MgO for package. The encapsulation efficiency was measured with ICP and calculated to be 65.90%; this meant that when 50 μl of MPs were injected, ~164.74 μg of MgO nanoparticles were injected, which is about eight times as many as in the in vitro studies.

First, 50 mg of PLGA was added to 1 ml of DCM in a glass tube. When PLGA was completely dissolved, MgO&SA (1 or 2.5 mg) was added to the PLGA solution. The mixture was sonicated for 10 min and stirred for 12 hours to achieve a uniform solution. To prevent evaporation, the level of DCM was marked, and additional solvent was added as needed.

We added 22.5 ml of TPGS solution (0.01% w/v) to a 100-ml glass beaker with stirring at 360 rpm. Simultaneously, 2 ml of TPGS (0.01% w/v) was added to a glass test tube. Holding the glass tube containing TPGS vertically and under high vortexing, a glass Pasteur pipette was used to gradually add the PLGA/MgO&SA solution dropwise into the TPGS solution in the glass tube, thereby forming an emulsion. After additional 15 s of vortexing, the glass tube with the emulsified polymer was immediately immersed in ice water and sonicated in three 10-s bursts. Each sonication was paused to allow the solution to cool down before proceeding. The sonicator settings were 40% amplitude for a 700-W sonicator, and about 1/8 size of the probe tip of device was kept in the emulsion during the sonication process.

Next, 1 to 2 ml of TPGS from the stirring solution was added to the emulsion using a glass Pasteur pipette to thin the emulsified polymer for easier pouring. The nanoparticles were then hardened by stirring for 3 hours at 60°C.

The hardened nanoparticles were collected and cleaned by centrifugation three times with water. The final pellet resuspension volume was 2 ml. The resulting product was either lyophilized or dispersed in water for future use. The prepared PLGA microspheres loaded with MgO&SA nanoparticles were labeled as MgO&SA@PLGA.

Degradation testing of MgO&SA@PLGA microspheres in vivo

To investigate the degradation behavior of MgO&SA@PLGA microspheres in vivo, we monitored the pH changes and Mg^{2+} release rate. In brief, 50 mg of MgO&SA@PLGA microspheres, 47.5 mg of PLGA, and 2.5 mg of MgO were encased into a dialysis bag (3500 Da), and, then, all samples were immersed into 20 ml of PBS at 37°C. The pH changes of the solution were detected using a pH meter. In addition, 200 μl of immersion solution aliquot was diluted 40 times to measure the concentration of Mg^{2+}. To maintain the total volume of the immersion solution, we added 200 μl of PBS.

Characterization of MgO&SA@PLGA microspheres

TEM images were recorded on a FEI TECNAI F20 TEM (FEI, USA) at an acceleration voltage of 200 kV. The surface morphology and element distribution of MgO&SA@PLGA microspheres were investigated using an SEM (XL30, Philips, The Netherlands) with EDS (S-2500C, Hitachi, Japan). To increase the conductivity of the samples, the microspheres were coated with gold by a sputter-coater (E1030, Hitachi, Tokyo, Japan). The XRD patterns were obtained at a speed of 2°/min on a diffractometer (Rigaku Ultima III, Japan) using Cu Kα radiation. We analyzed MgO&SA by FTIR spectroscopy (Spectrum 100, PerkinElmer, USA). Water CA measurements were performed with a CA meter (CA100C, Innuo Co., Ltd., China) after MgO&SA powder was pressed into tablets. The particle size distribution of MgO&SA in DCM was measured by DLS (Malvern ZetaSizer Nano ZS, Malvern, UK). A PHS-3C–type laboratory acidity meter was used to monitor the pH change in the process of immersion in vitro. The concentrations of Mg^{2+} in the immersion solution were determined using an inductively coupled plasma–optical emission spectrometer (Avio 500, PerkinElmer).

Cell culture

Primary human BMSCs and chondrocytes were isolated from clinical donors with the approval from the Ethics Committee of Nanjing Drum Tower Hospital. Primary bone marrow monocytes (BMMs) were isolated from 12-week-old C57BL/6 mice in a sterile environment. The ATDC5 and SW1353 cells, which are chondroblast and chondrocyte cell lines, respectively, were obtained from the Chinese Academy of Sciences Cell Bank. The cells were cultured in specific medium as follows: Dulbecco's modified Eagle's medium (DMEM) for ATDC5, primary chondrocytes, and BMSCs; DMEM/Ham's F-12 for SW1353; and DMEM/high glucose for monocytes. The media were supplemented with 10% fetal calf serum and 1% penicillin/streptomycin (Gibco, USA). The cells were cultured at 37°C with 5% CO_2, and the culture medium was changed every 2 to 3 days. Only cells in the exponential growth phase were used for the experiments.

Induction of chondrogenic, osteogenic, and osteoclastic differentiation

The culture medium was switched to chondrogenic, osteogenic, and osteoclastic media, as indicated in table S3, at the onset of differentiation. It is important to note that micro-mass culture is a specific method used for cultivating cartilage mass during chondrogenic differentiation. In brief, BMSCs were trypsinized and suspended at a density of 1×10^7 cells/ml in a chondrogenic differentiation medium. A 20-μl drop of the single-cell suspension was seeded at the bottom of each well in a 24-well plate. When the cells adhered to the bottom of the wells, the chondrogenic medium was added to reach a final volume of 500 μl per well. The evaluation indexes for differentiation are shown in table S3.

In the bone resorption experiment, calf bone slices (150 μm in thickness; Lushen biotechnology, China) were placed at the bottom of 96-well plates, and BMMs were seeded on the bone slices and incubated with conditional osteoclastic media for 7 days. After the cells were removed using an ultrasonic cleaner, the bone slices were fixed with 2.5% glutaraldehyde at 4°C for 2 hours and dehydrated using gradient alcohol. Then, the surface of the slices was observed using SEM.

Cell viability and proliferation

Cell viability was evaluated using a commercial cell counting kit-8 (CCK-8) kit. To evaluate cytotoxicity, the cells were seeded in 96-well plates and maintained at 70 to 80% confluence. To evaluate cell proliferation, the same number of cells were seeded initially in all holes, while cell confluence was kept at about 30%. After incubation with conditioned medium for 24 hours, the cells were washed three times with PBS. Subsequently, 200 μl of the complete medium was added to each well. Next, 20 μl of CCK-8 solution was introduced to each well using multiple pipettes. The plates were then incubated at 37°C for 2 hours. The absorbance at 450 nm (OD) was measured using a microplate reader, and cell viability was calculated using Eq. 1

$$\text{Cell viability}\ (\%) = \frac{OD_{exp} - OD_{sham}}{OD_{ctl} - OD_{sham}}(\%) \quad (1)$$

Cell staining

We conducted Alcian blue, ALP, ARS, and TRAP staining to confirm the differentiation of cells. Following fixation with 4% paraformaldehyde for 20 min, the corresponding commercial kits were used for staining. For Alcian blue staining, chondrocytes were dissolved in 7 M guanidine after staining. The absorbance of the solution was measured at 595 nm using a microplate reader (Multiskan GO, Thermo Fisher Scientific, USA). Calcium nodules stained with ARS were dissolved in 10% hexadecyl pyridinium chloride, and the absorbance of the solution was measured at 562 nm for quantification purposes. The positive area of ALP staining was quantified on microscopy images. Similarly, TRAP staining was quantified by measuring the number and area of osteoclasts.

Total RNA extraction, reverse transcription, and quantitative real-time PCR

mRNA extraction from cells and tissues was conducted using TRIzol following a standard protocol. The extracted mRNA was then identified and quantified using a spectrophotometer. Reverse transcription was carried out using the PrimeScript RT Reagent Kit (Takara, catalog no. RR037A) in accordance with the manufacturer's instructions. For quantitative polymerase chain reaction (PCR), we used 20 μl of reaction volume, which consisted of 7.8 μl of ribonuclease-free water, 10 μl of mix, 1 μl of diluted cDNA, 0.6 μl of forward primer, and 0.6 μl of reverse primer. The forward and reverse primers used in this work are listed in table S4. Quantitative PCR was performed on a LightCycler 480II (Roche, Switzerland) under the following parameters: initial denaturation at 94°C for 3 min, followed by cycles of denaturation at 94°C for 20 s, annealing at the primer-specific temperature for 20 s, and elongation at 72°C for 15 s. Cycle threshold values were recorded for subsequent analysis.

Preparation of protein samples and Western blotting

Cell and tissue protein samples were prepared using radioimmunoprecipitation assay (RIPA) lysis buffer containing cocktails. The tissues were snap-frozen with liquid nitrogen and, subsequently, ground to powder. The powder was mixed with RIPA lysis buffer, and the mixture was mixed with a homogenizer (Bioprep-24) by bead beating method. The cell lysates were prepared using an ultrasonic cell disruptor. Subsequently, the lysates were centrifuged at 13,000*g* for 20 min, and the supernatant was retained for further experiments. Protein concentration was determined using a bicinchoninic acid (BCA) kit (Thermo Fisher Scientific, catalog no. 23235) in accordance

with the manufacturer's instructions. The protein was then adjusted to a concentration of 1 μg/ml and mixed with loading buffer at 95°C for 10 min. Western blotting was carried out using a standard protocol, with the primary antibodies used listed in table S5. The gray value was measured using a Tanon 5200-Multi Chemiluminescent Imaging System (Tanon, China).

Cell apoptosis

After treatment with conditioned medium for 24 hours, cells were subjected to flow cytometry using a commercial kit [Becton, Dickinson and Company (BD), USA]. The cells collected by pancreatin without EDTA were mixed with the cell supernatant and then centrifuged at 1500*g* for 3 min. Then, the precipitated cells were washed with PBS three times and with binding buffer once. Following resuspension in binding buffer, propidine iodide (PI), and annexin V dye were added to the samples. The fluorescence intensity was lastly detected by flow cytometry (BD).

Tissue culture

Articular cartilage tissue was collected from 13 patients with OA diagnosed with Kellgren and Lawrence grade 4 OA by radiography according to the inclusion and exclusion criteria. During total knee arthroplasty, cartilage was obtained from the lesion area and transported to clean bench using ice boxes within 1 hour. The tissues were maintained in DMEM/Ham's F-12 medium supplemented with 10% fetal bovine serum and 1% penicillin/streptomycin. After treatment with conditioned medium, part of the tissues was used for frozen sections, and the other part was used for extracting protein. In the time course experiments, after treatment with conditioned medium for 0, 4, 12, and 72 hours, the tissues were used for paraffin embedding, immunostaining, and protein and mRNA extraction.

Animal management

A total of 24 8-week-old male rats were purchased from Beijing Vital River Laboratory Animal Technology Co. Ltd. (China). The rats were maintained in a specific pathogen–free environment, and feed and bedding were changed twice a week. Experimental protocols were reviewed and approved by the Drum Tower Hospital Ethics Committee (20180201).

Establishment of the rat OA model

The rats were anesthetized using isoflurane, and the right knee was chosen as the site of operation. Before fixation of the rats in the supine position, the skin in the surgical area was shaved. The medial collateral ligament was exposed and transected using micro-scissors, and muscles were dissected to achieve medial meniscectomy within the articular cavity. This procedure aimed to induce instability in the lower limbs. Following stratified saturation, radiography-assisted arthrocentesis was performed, and 50 μl of injectant was injected using a micro-injector. After a period of 4 weeks, the rats were euthanized with an overdose of anesthesia. Tissue samples from their right knee, heart, liver, lung, kidney, and blood were collected for subsequent experiments.

Histological section and staining analysis

The soft tissues (heart, liver, lung, kidney, and cartilage tissue) were prepared into frozen sections for H&E staining following a standard protocol. The knee joints were decalcified by 10% EDTA (pH 7.4) for 4 to 8 weeks after fixation in 4% paraformaldehyde for 48 hours. After gradient alcohol dehydration, the joints were embedded in paraffin. Ten-micrometer-thick coronal-oriented sections of the knee joint were processed for Safranin O/Fast Green staining and immunohistochemical staining using a standard protocol. The OARSI score was evaluated in a blinded fashion with two independent observers, and the average score was defined as the final score (ZEISS, Axio Lab A1).

Micro-CT analysis

High-resolution micro-CT (VivaCT 80, SCANCO Medical AG, Switzerland) was used to assess the subchondral bone. The scanning parameters were as follows: voltage of 45 kV, current of 177 μA, and voxel size of 15.6 μm. Sagittal images of the tibial subchondral bone were acquired for subsequent three-dimensional histomorphometric analysis. A region of interest measuring 312 μm (20 consecutive images) from the medial tibial plateau was defined. Only cancellous bone was included in the histological and morphological analysis, which encompassed the following parameters: the BMD of the TV and BV, the BV/TV, the trabecular spacing, the trabecular thickness, the structural model index, and the bone surface area–to–volume ratio. After excluding the maximum and minimum values, statistical analysis was conducted on six samples per group.

Undecalcified bone slicing and evaluation of bone formation

Nine rats were used to evaluate subchondral bone formation. Following the establishment of the OA model, separate intraperitoneal injections of calcein and xylenol orange were administered at 2 and 3 weeks, respectively. The right knee joints of the rats at the 4-week mark were used for undecalcified bone slicing. The tissues were fixed with 4% paraformaldehyde and subsequently dehydrated using alcohol gradient. After a 3-day immersion in curable resin with 70, 50, and 30% ethyl alcohol consecutively, the tissues were embedded in curable resin and solidified using light for ~12 hours. A hard-tissue slicer (EXAKT 310/36–00216, Germany) was used to grind the tissue blocks. Undecalcified bone slicing was performed, and the sections were observed under a fluorescence microscope using 10× and 40× objective lenses. The distance between the calcein and xylenol orange lines was measured five times per section, and, subsequently, the BFR was calculated as the distance divided by the interval time (7 days).

Behavioral tests

The behavioral tests, including gait measurement and von Frey test, were conducted at 2 and 4 weeks following the establishment of the OA model. In the gait measurement, the fore and rear foot were marked separately with red and blue, and the rats were placed on a straight track. The stride length and stepped length, as shown in Fig. 7A, were defined. Spatial symmetry was calculated using Eq.2, as per previous studies. A spatially symmetric gait was indicated by a spatial symmetry value close to 0, suggesting that the right foot was positioned between the two left feet.

In the von Frey test, the rats were placed in a quiet environment for over 30 min. Subsequently, a needle was used to apply increasing pressure to the right rear paw of each rat. The force at which the rat retracted its paw was recorded for further analysis. This test was repeated at least three times for each rat

$$\text{Spatial Symmetry} = \text{Abs}\left(\frac{\text{Step Length}}{\text{Stride Length}} - 0.5\right) \quad (2)$$

Statistical analysis

Statistical significance of differences between groups was assessed using one-way analysis of variance (ANOVA) followed by Tukey post hoc analysis (for more than two groups) and *t* test (for two groups). A *P* value lower than 0.05 was considered significant. Statistical analysis was conducted using SPSS 20.0, while GraphPad 9.0 was used to create the statistical graphs.

Supplementary Materials

This PDF file includes:

Figs. S1 to S11
Tables S1 to S5

REFERENCES AND NOTES

1. D. Prieto-Alhambra, A. Judge, M. K. Javaid, C. Cooper, A. Diez-Perez, N. K. Arden, Incidence and risk factors for clinically diagnosed knee, hip and hand osteoarthritis: Influences of age, gender and osteoarthritis affecting other joints. *Ann. Rheum. Dis.* **73**, 1659–1664 (2014).
2. L. Zou, K. Chu, X. He, Y. Li, L. Zhou, X. Xu, W. H. Liao, L. Qin, Hybrid therapeutic device (CUHK-OA-M2) for relieving symptoms induced by knee osteoarthritis. *Bioengineering* **10**, 95 (2023).
3. D. J. Hunter, D. Schofield, E. Callander, The individual and socioeconomic impact of osteoarthritis. *Nat. Rev. Rheumatol.* **10**, 437–441 (2014).
4. D. J. Hunter, S. Bierma-Zeinstra, Osteoarthritis. *Lancet* **393**, 1745–1759 (2019).
5. Z. Lv, Y. X. Yang, J. Li, Y. Fei, H. Guo, Z. Sun, J. Lu, X. Xu, Q. Jiang, S. Ikegawa, D. Shi, Molecular classification of knee osteoarthritis. *Front Cell Dev Biol* **9**, 725568 (2021).
6. Q. Yao, X. Wu, C. Tao, W. Gong, M. Chen, M. Qu, Y. Zhong, T. He, S. Chen, G. Xiao, Osteoarthritis: Pathogenic signaling pathways and therapeutic targets. *Signal Transduct. Target. Ther.* **8**, 56 (2023).
7. B. C. Geiger, S. Wang, R. F. Padera, A. J. Grodzinsky, P. T. Hammond, Cartilage-penetrating nanocarriers improve delivery and efficacy of growth factor treatment of osteoarthritis. *Sci. Transl. Med.* **10**, eaat8800 (2018).
8. K. Johnson, S. Zhu, M. S. Tremblay, J. N. Payette, J. Wang, L. C. Bouchez, S. Meeusen, A. Althage, C. Y. Cho, X. Wu, P. G. Schultz, A stem cell-based approach to cartilage repair. *Science* **336**, 717–721 (2012).
9. L. Zhou, P. Guo, M. D'Este, W. Tong, J. Xu, H. Yao, M. J. Stoddart, G. J. V. M. van Osch, K. K. W. Ho, Z. Li, L. Qin, Functionalized hydrogels for articular cartilage tissue engineering. *Engineering* **13**, 71–90 (2022).
10. L. Zhou, V. O. Gjvm, J. Malda, M. J. Stoddart, Y. Lai, R. G. Richards, K. Ki-wai Ho, L. Qin, Innovative tissue-engineered strategies for osteochondral defect repair and regeneration: Current progress and challenges. *Adv. Healthc. Mater.* **9**, e2001008 (2020).
11. L. Mao, W. Wu, M. Wang, J. Guo, H. Li, S. Zhang, J. Xu, J. Zou, Targeted treatment for osteoarthritis: Drugs and delivery system. *Drug Deliv.* **28**, 1861–1876 (2023).
12. M. J. Richard, J. B. Driban, T. E. McAlindon, Pharmaceutical treatment of osteoarthritis. *Osteoarthr. Cartil.* **31**, 458–466 (2023).
13. Y. Li, S. Zhao, S. Li, Y. Ge, R. Wang, L. Zheng, J. Xu, M. Sun, Q. Jiang, Y. Zhang, H. Wei, Surface engineering of biodegradable magnesium alloys for enhanced orthopedic implants. *Small* **15**, e1904486 (2019).
14. J. Xu, P. Hu, X. Zhang, J. Chen, J. Wang, J. Zhang, Z. Chen, M. K. Yu, Y. W. Chung, Y. Wang, X. Zhang, Y. Zhang, N. Zheng, H. Yao, J. Yue, H. C. Chan, L. Qin, Y. C. Ruan, Magnesium implantation or supplementation ameliorates bone disorder in CFTR-mutant mice through an ATF4-dependent Wnt/β-catenin signaling. *Bioact. Mater.* **8**, 95–108 (2022).
15. B. Dai, X. Li, J. Xu, Y. Zhu, L. Huang, W. Tong, H. Yao, D. H.-K. Chow, L. Qin, Synergistic effects of magnesium ions and simvastatin on attenuation of high-fat diet-induced bone loss. *Bioact. Mater.* **6**, 2511–2522 (2021).
16. Y. Zhang, J. Xu, Y. C. Ruan, M. K. Yu, M. O'Laughlin, H. Wise, D. Chen, L. Tian, D. Shi, J. Wang, S. Chen, J. Q. Feng, D. H. K. Chow, X. Xie, L. Zheng, L. Huang, S. Huang, K. Leung, N. Lu, L. Zhao, H. Li, D. Zhao, X. Guo, K. Chan, F. Witte, H. C. Chan, Y. Zheng, L. Qin, Implant-derived magnesium induces local neuronal production of CGRP to improve bone-fracture healing in rats. *Nat. Med.* **22**, 1160–1169 (2016).
17. Y. Li, J. Yue, C. Yang, Unraveling the role of Mg^{++} in osteoarthritis. *Life Sci.* **147**, 24–29 (2016).
18. R. Bai, M. Z. Miao, H. Li, Y. Wang, R. Hou, K. He, X. Wu, H. Jin, C. Zeng, Y. Cui, G. Lei, Increased Wnt/β-catenin signaling contributes to autophagy inhibition resulting from a dietary magnesium deficiency in injury-induced osteoarthritis. *Arthritis Res. Ther.* **24**, 165 (2022).
19. X. Kuang, J. Chiou, K. Lo, C. WEN, Magnesium in joint health and osteoarthritis. *Nutr. Res.* **90**, 24–35 (2021).
20. C. H. Lee, Z. H. Wen, Y. C. Chang, S. Y. Huang, C. C. Tang, W. F. Chen, S. P. Hsieh, C. S. Hsieh, Y. H. Jean, Intra-articular magnesium sulfate ($MgSO_4$) reduces experimental osteoarthritis and nociception: Association with attenuation of *N*-methyl-d-aspartate (NMDA) receptor subunit 1 phosphorylation and apoptosis in rat chondrocytes. *Osteoarthr. Cartil.* **17**, 1485–1493 (2009).
21. H. Yao, J. K. Xu, N. Y. Zheng, J. L. Y. L. Y. Wang, S. W. Mok, Y. W. Lee, L. Shi, J. L. Y. L. Y. Wang, J. Yue, S. H. Yung, P. J. Hu, Y. C. Ruan, Y. F. Zhang, K. W. Ho, L. Qin, Intra-articular injection of magnesium chloride attenuates osteoarthritis progression in rats. *Osteoarthr. Cartil.* **27**, 1811–1821 (2019).
22. S. Glyn-Jones, A. J. R. Palmer, R. Agricola, A. J. Price, T. L. Vincent, H. Weinans, A. J. Carr, Osteoarthritis. *Lancet* **386**, 376–387 (2015).
23. F.-Y. Li, B. Chaigne-Delalande, C. Kanellopoulou, J. C. Davis, H. F. Matthews, D. C. Douek, J. I. Cohen, G. Uzel, H. C. Su, M. J. Lenardo, Second messenger role for Mg^{2+} revealed by human T-cell immunodeficiency. *Nature* **475**, 471–476 (2011).
24. L. Z. Zheng, J. L. Wang, J. K. Xu, X. T. Zhang, B. Y. Liu, L. Huang, R. Zhang, H. Y. Zu, X. He, J. Mi, Q. Q. Pang, X. L. Wang, Y. C. Ruan, D. W. Zhao, L. Qin, Magnesium and vitamin C supplementation attenuates steroid-associated osteonecrosis in a rat model. *Biomaterials* **238**, 119828 (2020).
25. J. Liu, H. Zeng, P. Xiao, A. Yang, X. Situ, Y. Wang, X. Zhang, W. Li, W. Pan, Y. Wang, Sustained release of magnesium ions mediated by a dynamic mechanical hydrogel to enhance BMSC proliferation and differentiation. *ACS Omega* **5**, 24477–24486 (2020).
26. Z. Liao, L. Fu, P. Li, J. Wu, X. Yuan, C. Ning, Z. Ding, X. Sui, S. Liu, Q. Guo, Incorporation of magnesium ions into an aptamer-functionalized ECM bioactive scaffold for articular cartilage regeneration. *ACS Appl. Mater. Interfaces* **15**, 22944–22958 (2023).
27. A. Shmagel, N. Onizuka, L. Langsetmo, T. Vo, R. Foley, K. Ensrud, P. Valen, Low magnesium intake is associated with increased knee pain in subjects with radiographic knee osteoarthritis: Data from the Osteoarthritis Initiative. *Osteoarthr. Cartil.* **26**, 651–658 (2018).
28. B. Qin, X. Shi, P. S. Samai, J. B. Renner, J. M. Jordan, K. He, Association of dietary magnesium intake with radiographic knee osteoarthritis: Results from a population-based study. *Arthritis Care Res.* **64**, 1306–1311 (2012).
29. L. Zhou, J. Xu, A. Schwab, W. Tong, J. Xu, L. Zheng, Y. Li, Z. Li, S. Xu, Z. Chen, L. Zou, X. Zhao, G. J. V. M. van Osch, C. Wen, L. Qin, Engineered biochemical cues of regenerative biomaterials to enhance endogenous stem/progenitor cells (ESPCs)-mediated articular cartilage repair. *Bioact. Mater.* **26**, 490–512 (2023).
30. K. Sun, J. Luo, J. Guo, X. Yao, X. Jing, F. Guo, The PI3K/AKT/mTOR signaling pathway in osteoarthritis: A narrative review. *Osteoarthr. Cartil.* **28**, 400–409 (2020).
31. D. B. Burr, M. A. Gallant, Bone remodelling in osteoarthritis. *Nat. Rev. Rheumatol.* **8**, 665–673 (2012).
32. W. Hu, Y. Chen, C. Dou, S. Dong, Microenvironment in subchondral bone: Predominant regulator for the tr eatment of osteoarthritis. *Ann. Rheum. Dis.* **80**, 413–422 (2023).
33. G. Amir, C. J. Pirie, S. Rashad, P. A. Revell, Remodelling of subchondral bone in osteoarthritis: A histomorphometric study. *J. Clin. Pathol.* **45**, 990–992 (1992).
34. Z. Cui, J. Crane, H. Xie, X. Jin, G. Zhen, C. Li, L. Xie, L. Wang, Q. Bian, T. Qiu, M. Wan, M. Xie, S. Ding, B. Yu, X. Cao, Halofuginone attenuates osteoarthritis by inhibition of TGF-β activity and H-type vessel formation in subchondral bone. *Ann. Rheum. Dis.* **75**, 1714–1721 (2016).
35. W. Liu, C. C. Le, D. Wang, D. Ran, Y. Wang, H. Zhao, J. Gu, H. Zou, Y. Yuan, J. Bian, Z. Liu, Ca^{2+}/CaM/CaMK signaling is involved in cadmium-induced osteoclast differentiation. *Toxicology* **441**, 152520 (2020).
36. K. Sato, A. Suematsu, T. Nakashima, S. Takemoto-Kimura, K. Aoki, Y. Morishita, H. Asahara, K. Ohya, A. Yamaguchi, T. Takai, T. Kodama, T. A. Chatila, H. Bito, H. Takayanagi, Regulation of osteoclast differentiation and function by the CaMK-CREB pathway. *Nat. Med.* **12**, 1410–1416 (2006).
37. Y. S. Lee, Y. S. Kim, S. Y. Lee, G. H. Kim, B. J. Kim, S. H. Lee, K. U. Lee, G. S. Kim, S. W. Kim, J. M. Koh, AMP kinase acts as a negative regulator of RANKL in the differentiation of osteoclasts. *Bone* **47**, 926–937 (2010).
38. R. Kamada, F. Kudoh, S. Ito, I. Tani, J. I. B. Janairo, J. G. Omichinski, K. Sakaguchi, Metal-dependent Ser/Thr protein phosphatase PPM family: Evolution, structures, diseases and inhibitors. *Pharmacol. Ther.* **215**, 107622 (2020).
39. W. Chen, S. Wang, J. Xia, Z. Huang, X. Tu, Z. Shen, Protein phosphatase 2A plays an important role in migration of bone marrow stroma cells. *Mol. Cell. Biochem.* **412**, 173–180 (2016).
40. H. E. Broxmeyer, J. Ropa, M. L. Capitano, S. Cooper, L. Racioppi, U. Sankar, CaMKK2 knockout bone marrow cells collected/processed in low oxygen (Physioxia) suggests CaMKK2 as a hematopoietic stem to progenitor differentiation fate determinant. *Stem Cell Rev. Rep.* **18**, 2513–2521 (2022).
41. W.-L. Wan, Y.-J. Lin, P.-C. Shih, Y.-R. Bow, Q. Cui, Y. Chang, W.-T. Chia, H.-W. Sung, An in situ depot for continuous evolution of gaseous H_2 med iated by a magnesium passivation/activation cycle for treating osteoar thritis. *Angew. Chem. Int. Ed. Engl.* **57**, 9875–9879 (2023).
42. Z. Yuan, P. Wei, Y. Huang, W. Zhang, F. Chen, X. Zhang, J. Mao, D. Chen, Q. Cai, X. Yang, Injectable PLGA microspheres with tunable magnesium ion release for promoting bone regeneration. *Acta Biomater.* **85**, 294–309 (2019).

43. Z. Lin, J. Wu, W. Qiao, Y. Zhao, K. H. M. M. Wong, P. K. Chu, L. Bian, S. Wu, Y. Zheng, K. M. C. C. Cheung, F. Leung, K. W. K. K. Yeung, Precisely controlled delivery of magnesium ions thru sponge-like monodisperse PLGA/nano-MgO-alginate core-shell microsphere device to enable in-situ bone regeneration. *Biomaterials* **174**, 1–16 (2018).
44. E. Albrecht, K. R. Kirkham, S. S. Liu, R. Brull, Peri-operative intravenous administration of magnesium sulphate and postoperative pain: A meta-analysis. *Anaesthesia* **68**, 79–90 (2013).
45. M. Hou, Y. Zhang, X. Zhou, T. Liu, H. Yang, X. Chen, F. He, X. Zhu, Kartogenin prevents cartilage degradation and alleviates osteoarthritis progression in mice via the miR-146a/NRF2 axis. *Cell Death Dis* **12**, 483 (2021).
46. Q. Sun, G. Zhen, T. P. Li, Q. Guo, Y. Li, W. Su, P. Xue, X. Wang, M. Wan, Y. Guan, X. Dong, S. Li, M. Cai, X. Cao, Parathyroid hormone attenuates osteoarthritis pain by remodeling subchondral bone in mice. *eLife* **10**, e66532 (2021).
47. W. Pei, Y. Yusufu, Y. Zhan, X. Wang, J. Gan, L. Zheng, P. Wang, K. Zhang, C. Huang, Biosynthesizing lignin dehydrogenation polymer to fabricate hybrid hydrogel composite with hyaluronic acid for cartilage repair. *Adv. Compos. Hybrid Mater.* **6**, 180 (2023).

Acknowledgments: We thank LetPub (www.letpub.com) for its linguistic assistance during the preparation of this manuscript. We appreciated all staffs in our departments for the assistant in completing the work. **Funding:** This work was supported by National Key Research and Development Project (2021YFA1201404), the Central Government of China (Q.J.); Major Project (81991514), National Natural Science Foundation of China (Q.J.); National Science Foundation for Youths (82202778), National Natural Science Foundation of China (Y.L.); General Program (2022 M722769), China Postdoctoral Science Foundation (L.Z.); and Jiangsu Provincial Key R&D Program (BE2022836), National Key R&D Program of China (2019YFA0709200 and 2021YFF1200700), Fundamental Research Funds for the Central Universities (202200325), and State Key Laboratory of Analytical Chemistry for Life Science (5431ZZXM2306) (H.W.). **Author contributions:** Conceptualization: L.Z., S.Z., Y.L., Y.Z., H.W., and Q.J. Methodology: L.Z., S.Z., and Y.L. Investigation: Jiankun Xu, B.G., Jianbin Xu, L.J., and W.Y. Visualization: Jiankun Xu, B.G., Jianbin Xu, L.J., and W.Y. Supervision: H.W., Q.J., and Y.Z. Writing—original draft: L.Z., S.Z., and Y.L. Writing—review and editing: Y.Z., H.W., and Q.J. **Competing interests:** The authors declare that they have no competing interests. **Data and materials availability:** All data needed to evaluate the conclusions in the paper are present in the paper and/or the Supplementary Materials.

Submitted 31 August 2023
Accepted 2 February 2024
Published 8 March 2024
10.1126/sciadv.adk6084